iScience

CellPress
OPEN ACCESS

Article

Two-color electromagnetically induced transparency generated slow light in double-mechanical-mode coupling carbon nanotube resonators

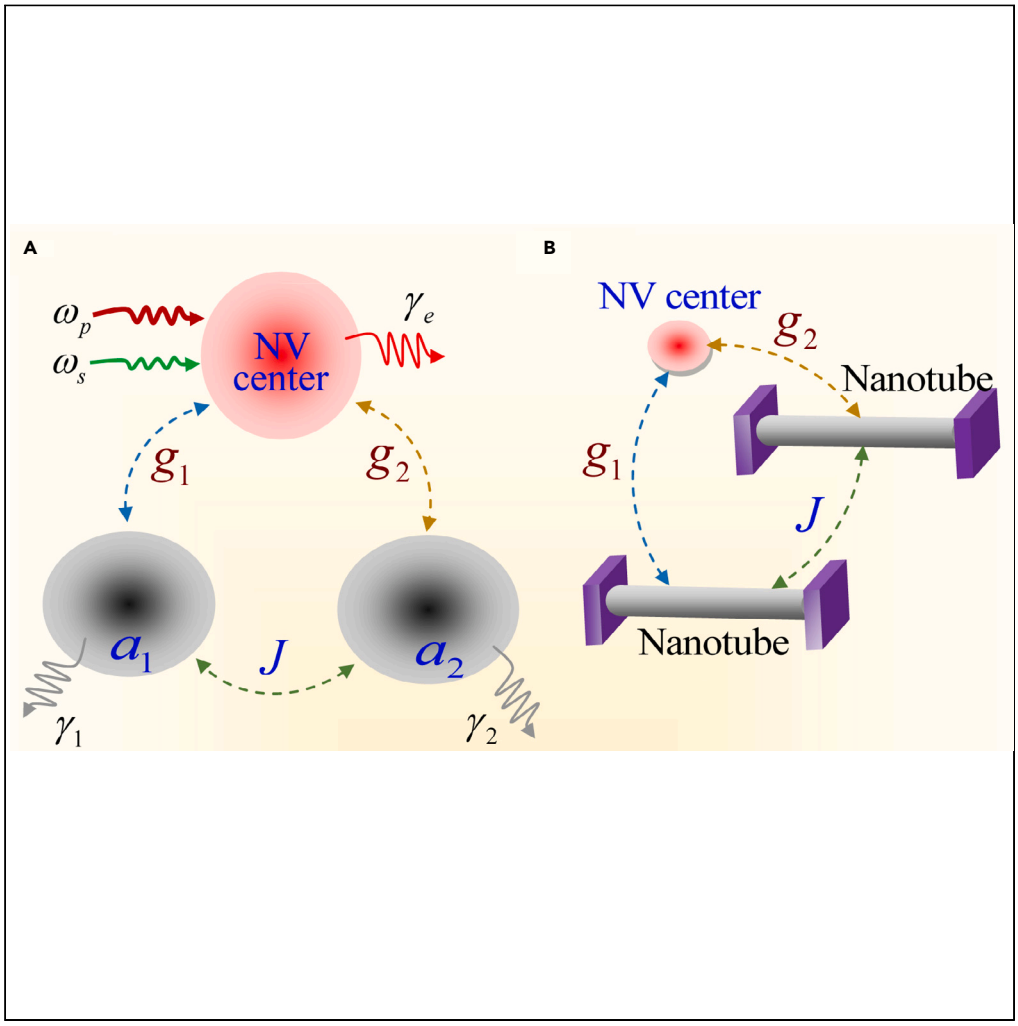

Hua-Jun Chen

chenphysics@126.com

Highlights

A multimode nanoresonators coupled system is proposed by phonon-exchange interaction

Two-color EIT can be achieved by controlling different coupling regimes

The slow light can be controlled periodically by tuning the modulation phase

Increasing resonators number, intricate resonator networks become attainable

Chen, iScience 27, 109328
April 19, 2024
https://doi.org/10.1016/j.isci.2024.109328

iScience

CellPress
OPEN ACCESS

Article

Two-color electromagnetically induced transparency generated slow light in double-mechanical-mode coupling carbon nanotube resonators

Hua-Jun Chen[1,2,3,*]

SUMMARY

We theoretically propose a multiple-mode-coupling hybrid quantum system comprising two-mode-coupling nanomechanical carbon nanotube (CNT) resonators realized by a phase-dependent phonon-exchange interaction interacting with the same nitrogen-vacancy (NV) center in diamond. We investigate the coherent optical responses of the NV center under the condition of resonance and detuning. In particular, two-color electromagnetically induced transparency (EIT) can be achieved by controlling the system parameters and coupling regimes. Combining the spin-phonon interactions and phonon-phonon coupling with the modulation phase, the switching of one and two EIT windows has been demonstrated, which generates a light delay or advance. The slow-to-fast and fast-to-slow light transitions have been studied in different coupling regimes, and the switch between slow and fast light can be controlled periodically by tuning the modulation phase. The study can be applied to phonon-mediated optical information storage or information processing with spin qubits based on multiple-mode hybrid quantum systems.

INTRODUCTION

Hybrid quantum systems interfacing absolutely diverse physical components can carry out novel functionalities that individual systems cannot own,[1,2] which has attracted tremendous attention for investigating quantum phenomena and developing quantum technologies[1] in the past few decades. In recent years, combining solid-state systems with quantum nanomechanical systems has received great interest. Solid-state systems can be two-level systems (TLSs) (such as superconducting qubits,[3] defects in semiconductors,[4] atoms,[5] and quantum dots[6,7]) and solid-state spins.[8,9] Given the long coherence time of solid-state spins,[10–12] representative hybrid quantum systems, that is, hybrid spin-mechanical systems,[13–18] have been extensively applied because they can take full advantage of the excellent properties of solid-state spins and high quality (Q) factors of nanomechanical resonators (NRs),[19] ranging from quantum sensing to quantum information processing.[20] For nanomechanical systems,[21] given their fascinating properties of ultralow mass, ultrahigh and extensively tunable frequencies, and ultrahigh Q factors, carbon nanotubes (CNTs) make them perfect nanomechanical devices, such as ultrasensitive interferometers and sensing devices.[22–25]

To establish spin-mechanical devices, solid-state spin qubits such as nitrogen-vacancy (NV) defect-center spins in diamond[26–29] coupling to nanomechanical resonators are leading candidates for hybrid spin-mechanical devices because they take advantage of the long coherence time of NV spins even at room temperature[10–12] and enormous Q factors of NRs, where the coupling of NV spins in diamond between mechanical resonators can be achieved extrinsically (such as external magnetic field gradients[4,11–14,17,30,31]) or intrinsically (such as mechanical strain[32–37]). For the first coupling case, the interaction comes from the relative motion of the NV spin and magnetic-field gradients,[13,38] where a magnetic tip is installed on a cantilever, generating magnetic coupling between the NV spin and NR.[4,11–14,17,30,31] For the second coupling case, the interaction of the NV spin and NR is derived from the crystal strain during mechanical motion.[6,32–35,37] However, for these two types of interactions, reaching the strong-coupling regime is still challenging. Recently, a spin-nanomechanical hybrid device achieving a strong-coupling regime has been presented, where the NV center in diamond is interfaced with a suspended CNT carrying a dc current.[39]

On the other hand, mode coupling of mechanical resonators, due to its enormous advantage for fundamental studies and practical device applications at micro-nanoscale,[25,40–44] has attracted numerous attention in recent years. To date, three representative strong mode-coupling regimes have been demonstrated experimentally: the linear mode coupling,[45] nonlinear strong mode coupling,[46,47] and dynamical strong mode coupling.[40,48,49] Given mechanical mode coupling, phonon Rabi oscillations,[49] coherent phonon manipulation,[50] spin-phonon interfaces,[51] mechanical PT symmetry,[52] and Fano resonance in multiple NRs[53] have been investigated in different mechanical systems. In addition, the analogous three-mode coupling hybrid systems have also been demonstrated in multimode optomechanical systems, which include one mechanical mode coupled to two cavity modes by radiation pressure[54–59] and a single optical mode coupled to mechanical modes.[60,61]

[1]School of Mechanics and Photoelectric Physics, Anhui University of Science and Technology, Huainan, Anhui 232001, China
[2]Center for Fundamental Physics, Anhui University of Science and Technology, Huainan, Anhui 232001, China
[3]Lead contact
*Correspondence: chenphysics@126.com
https://doi.org/10.1016/j.isci.2024.109328

Inspired by the outstanding properties of NV centers in diamond (such as the long coherence time even at room temperature and high controllability[62–64]) and unrivalled mechanical characteristics of CNTs (such as ultrahigh resonance frequencies and ultrahigh Q factors[22,23,25]), as well as the mechanical mode coupling,[40,48,49,51,52] we propose a two-mechanical-mode-coupling CNT resonator coupled to the same NV spin in diamond by magnetic-field gradients to form a hybrid quantum nanomechanical system. This arrangement engenders a hybrid quantum nanomechanical system, wherein the interactions among the CNT resonators are mediated by phase-dependent phonon-phonon interactions.[65] The proposed hybrid system is analogous three-mode coupling optomechanical system consisting of an optical cavity coupled to mechanical modes, and compared with hybrid optomechanical system, the NV spin in diamond can be replaced by other TLSs (such as superconducting qubits,[3] defects in semiconductors,[4] atoms,[5] and quantum dots[6]) and nanomechanical systems such as doubly clamped NR,[66] cantilever resonators,[38,51] and two-dimensional drum resonators[41,44] can also replace CNT resonators. By scaling up the number of CNT resonators, intricate spin-mechanical resonator networks become attainable.

In this study, using two-tone fields to drive the NV spin, the probe absorption spectra of the NV spin under the condition of resonance and detuning are investigated under different parametric regimes, such as spin-phonon coupling, different frequencies of CNT resonators, phonon-phonon coupling, and controlled phase of the phonon-phonon interaction. By controlling the parametric regimes, the probe absorption spectra manifest the phenomenon of electromagnetically induced transparency (EIT)[67]; in particular, the EIT with a single window turns into one with two windows (i.e., the two-color EIT[68]) by manipulating the spin-phonon coupling and the frequencies of CNT resonators. The phenomenon of two-color EIT is concomitant with rapid normal dispersion, engendering either a delay or advancement in light propagation. Expressly, a two-color EIT generated light delay or advance has been achieved, which can be manipulated and switched periodically by tuning the modulation phase. The proposed hybrid mechanical system is a promising integration platform for the optical storage or quantum communication.

RESULTS

We used the following parameters for the system[39,69–71]: $\omega_1 = \omega_2 = 65$ MHz, $g_1 = g_2 = 4.5$ MHz, $\gamma_1 = \gamma_2 = 15$ kHz, $\Omega_p = 10$ (MHz)^2, $\gamma_e = 60$ MHz, $J \sim [10, 100]$ MHz, and $\theta \in [0, 2\pi]$. Furthermore, nanomechanical resonators with high frequencies ranging from 100 MHz to a few GHz have been realized in the mechanical devices with smaller sizes or greater stiffness.[25,72,73]

The case of resonance: $\Delta_p = 0$

In this subsection, we investigate the coherent optical responses of the NV spin in the case of resonance, that is, $\Delta_p = 0$. Figure 1A shows the probe absorption of the NV spin with respect to $\Delta_s = \omega_s - \omega_e$ for three coupling regimes, that is, ($g_2 = 0, J = 0$), ($g_2 \neq 0, J = 0$), and ($g_2 \neq 0, J \neq 0$) at a fixed coupling strength $g_1 = 4.5$ MHz, Figure 1A1 shows the amplification of the right absorption peaks in Figure 1A. In the coupling regime of ($g_2 = 0, J = 0$), the system is a typical two-mode coupled system, that is, an NV spin is coupled to a phonon mode, and the probe absorption exhibits mode splitting, where the two absorption peaks are located at $\Delta_s = 0$ and $\Delta_s = \omega_1 = 65$ MHz, respectively. If another CNT resonator is considered, that is, the coupling regime becomes ($g_2 \neq 0, J = 0$), where an NV spin is simultaneously coupled to two CNT resonators with spin-phonon coupling strengths $g_1 = 4.5$ MHz and $g_2 = 4.5$ MHz, we find that the width of the two absorption peaks is broadened compared with the coupling regime of ($g_2 = 0, J = 0$) as shown by the red curve in Figure 1A. In the coupling regime of ($g_2 \neq 0, J \neq 0$), that is, the two CNT resonators are not only coupled to the same NV spin, but also the two CNT resonators can interact with each other with coupling strength $J = 20$ MHz, it is obvious that three absorption peaks located at $\Delta_s = 0$, $\Delta_s = \omega_1 - J$, and $\Delta_s = \omega_1 + J$, respectively, appear in the probe absorption. In particular, the two absorption peaks located at $\Delta_s = \omega_1 \pm J$ as shown by the blue curve, can be considered as the splitting of the single absorption peak located at $\Delta_s = \omega_1$ when the phonon-phonon coupling J is considered. Figure 1B gives the probe absorption for different frequencies of the CNT resonators without considering the phonon-phonon coupling ($J = 0$). If the two CNT resonators are identical (i.e., $\omega_2 = \omega_1 = 65$ MHz), the right single absorption peak located at $\Delta_s = \omega_1$ shows a Fano-like resonance, as shown by the black curve in Figure 1B1. Fano resonance was first discovered by Fano,[74] which exhibits a asymmetric feature of a photoionization cross section in atomic systems generated by the scattering of the light amplitude when the extra frequency detuning is introduced. However, in our system, we can obtain the Fano-like resonance even in the condition of $\Delta_p = 0$. If the two CNT resonators have different frequencies, there are two cases: $\omega_2 < \omega_1$ and $\omega_2 > \omega_1$. When $\omega_2 < \omega_1$ ($\omega_1 = 65$ MHz and $\omega_2 = 60$ MHz), the single Fano-like resonance located at $\Delta_s = \omega_1$ is split into double Fano-like resonance locating at $\Delta_s = \omega_2 = 60$ MHz and $\Delta_s = \omega_1 = 65$ MHz, respectively. When $\omega_2 > \omega_1$ ($\omega_1 = 65$ MHz, $\omega_2 = 70$ MHz), the single Fano-like resonance located at $\Delta_s = \omega_1$ in the probe absorption is also split into a double Fano-like resonance locating at $\Delta_s = \omega_1 = 65$ MHz and $\Delta_s = \omega_2 = 70$ MHz, respectively. Fano resonance induced applications, such as sensors,[75] enhanced light emission,[76] electromagnetically induced absorption,[77] and the slow light,[78] have been investigated in different systems.

In addition, the probe absorption spectra for different frequencies of CNT resonators with taking into consideration of the phonon-phonon coupling ($J = 20$ MHz) are also demonstrated as shown in Figures 1C and 1C1 shows the amplification of the right two Fano-like resonance peaks. Three absorption peaks appear in the probe absorption spectrum, and the right two absorption peaks present double Fano-like resonance. If the two CNT resonators have the same frequencies, indicated by the red curve in Figure 1C, the two Fano-like resonance peaks are located at. $\Delta_s = \omega_1 \pm J$. (or $\Delta_s = \omega_2 \pm J$), that is, $\Delta_s = \omega_1 - J = 45$ MHz and $\Delta_s = \omega_1 + J = 85$ MHz. However, if the two CNT resonators are different resonators with different frequencies, the two Fano-like resonance peaks are located at $\Delta_s = \overline{\omega} \pm J$, where $\overline{\omega} = (\omega_1 + \omega_2)/2$. For example, if $\omega_1 = 65$ MHz and $\omega_2 = 60$ MHz, the two Fano-like resonance peaks will locate at $\Delta_s = \overline{\omega} - J = 42.5$ MHz and $\Delta_s = \overline{\omega} + J = 82.5$ MHz with $\overline{\omega} = 62.5$ MHz, while if $\omega_1 = 65$ MHz and $\omega_2 = 70$ MHz, the two Fano-like resonance peaks will locate at $\Delta_s = \overline{\omega} - J = 47.5$ MHz and $\Delta_s = \overline{\omega} + J = 87.5$ MHz with $\overline{\omega} = 67.5$ MHz. Furthermore, the probe absorption spectra for different phonon-phonon coupling strengths

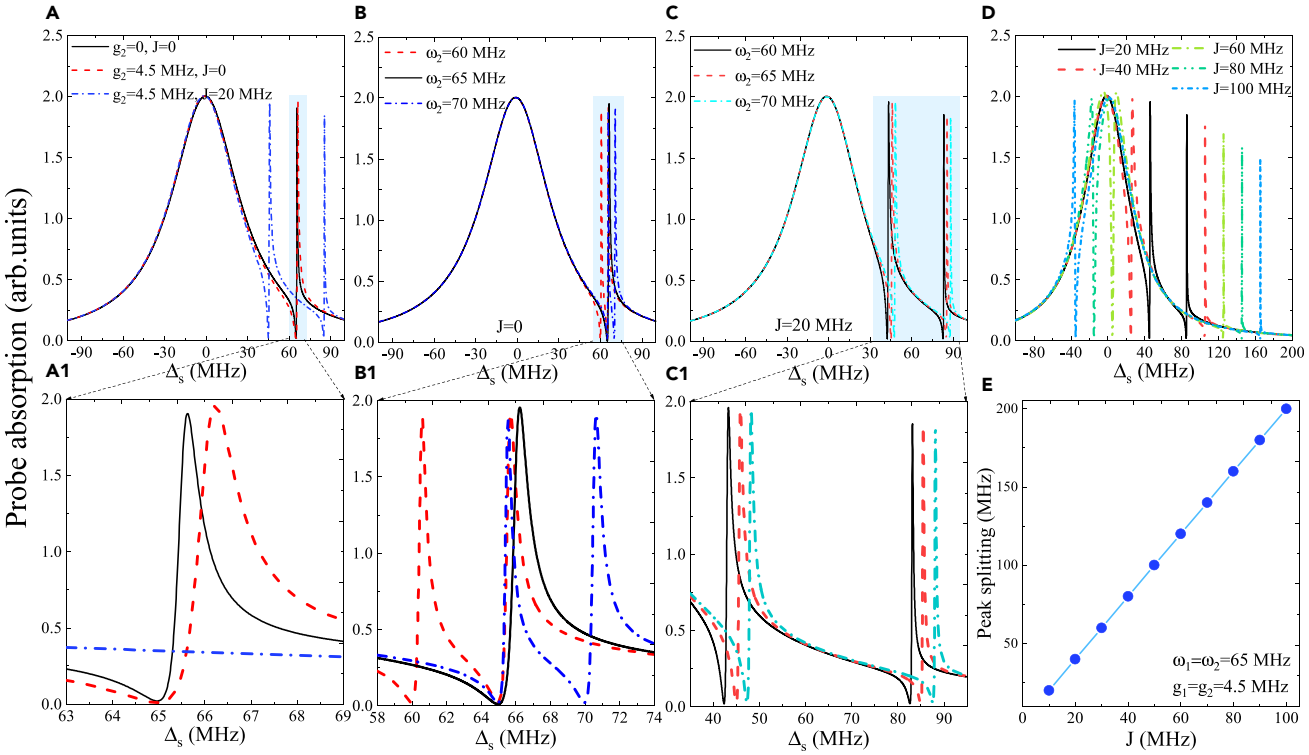

Figure 1. The probe absorption for different coupling regimes in the case of $\Delta_p = 0$

(A) The probe absorption of the NV spin with respect to Δ_s for three coupling regimes of ($g_2 = 0, J = 0$), ($g_2 \neq 0, J = 0$), and ($g_2 \neq 0, J \neq 0$) at $g_1 = 4.5$ MHz. (A1) The amplified parts in (A).

(B) The probe absorption for different frequencies of the CNT resonators at $J = 0$. (B1) The amplified parts in (B).

(C) The probe absorption for different frequencies of the CNT resonators at $J = 20$ MHz. (C1) The amplified parts in (C).

(D) The probe absorption spectra for different J with parameters $\omega_1 = \omega_2$, $g_1 = g_2$, and $\theta = \pi/2$.

(E) The splitting width of the double peaks as a function of the coupling strength J.

J in the parameters of $\omega_1 = \omega_2$, $g_1 = g_2$, and $\theta = \pi/2$ were also investigated, as shown in Figure 1D. We can see that the splitting width of the double Fano-like resonance is enhanced by increasing the phonon-phonon coupling strength J, and Figure 1E shows the splitting width of the double Fano-like resonance peaks as a function of the phonon-phonon coupling strength J, which indicates that the splitting width is proportional to the coupling strength J.

As shown in Figure 1D, if the phonon-phonon coupling strength J reaches to $J \sim \omega_1$, such as $J = 60$ MHz, the left Fano-like resonance peak located at $\Delta_s = \omega_1 - J$ will move to the left and arrive at $\Delta_s \approx 0$, then the probe absorption peak at $\Delta_s = 0$ splits into two peaks. Figure 2A presents the probe absorption as a function of Δ_s for different modulation phases θ in parametric regimes of $\omega_1 = \omega_2$, $g_1 = g_2$, and $J = 60$ MHz, Figure 2A1 shows the amplifying details of the probe absorption located at $\Delta_s = \omega_1 - J$ and Figure 2A2 shows the amplifying details located at $\Delta_s = \omega_1 + J$. According to Figures 2A and 21D, we can obtain the following results: (1) A broad absorption peak located at $\Delta_s \approx 0$ in the probe absorption is unchanged even increasing the phonon-phonon coupling strength; (2) In the presence of coupling strength J, two Fano-like resonance peaks located at $\Delta_s = \omega_1 \pm J$ appear in the probe absorption, and with increasing the coupling strength J, the left Fano-like resonance peaks move to the left and right Fano-like resonance peaks move to the right; (3) The linewidth of the two Fano-like resonance peaks located at $\Delta_s = \omega_1 \pm J$ is narrower than the broad absorption peak located at $\Delta_s \approx 0$. (4) When the phonon-phonon coupling strength J reaches to $J = \omega_1$ or $J \approx \omega_1$, the Fano-like resonance peak located at $\Delta_s = \omega_1 - J$ move to the location of the broad absorption peak located at $\Delta_s \approx 0$, and as a result, the broad absorption peak located at $\Delta_s \approx 0$ displays quasisymmetry splitting. However, there is a special situation, that is, modulation phase $\theta = 0$ or $\theta = \pi$ as shown in Figure 2B. In the condition of $\theta = 0$, the left Fano-like resonance located at $\Delta_s = \omega_1 - J$ disappears and only the right Fano resonance located at $\Delta_s = \omega_1 + J$ appears in the probe absorption. If $\theta = \pi$, the left Fano resonance located at $\Delta_s = \omega_1 - J$ moves to the left, which causes the broad absorption peak located at $\Delta_s = 0$ to present mode splitting, and the right Fano resonance located at $\Delta_s = \omega_1 + J$ disappears.

The case of detuning: $\Delta_p \neq 0$

In this subsection, we investigate the coherent optical responses of the NV spin in the case of red-detuning, that is, $\Delta_p = \omega_1$. Figure 3A plots the probe absorption of the NV spin with respect to Δ_s for three coupling regimes, i.e., ($g_2 = 0, J = 0$), ($g_2 \neq 0, J = 0$), and ($g_2 \neq 0,$

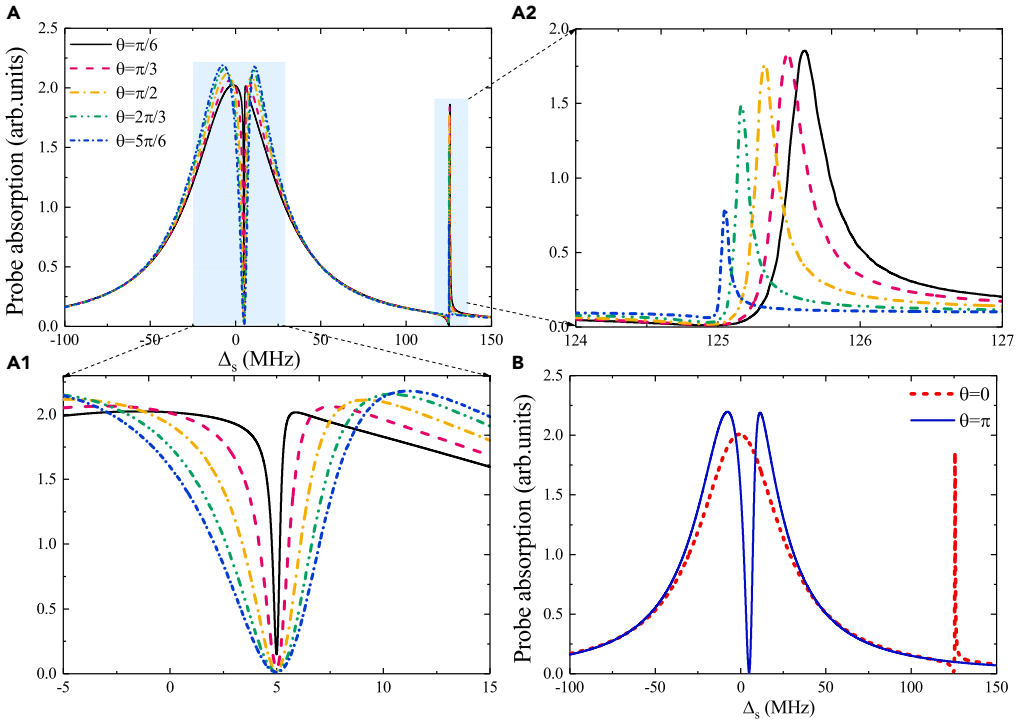

Figure 2. The probe absorption for different modulation phase θ at $\Delta_p = 0$

(A) The probe absorption versus Δ_s for different modulation phase θ with parametric $\omega_1 = \omega_2$, $g_1 = g_2$, and J = 60 MHz. (A1) and (A2) The amplifying details in (A).

(B) The probe absorption for the phase $\theta = 0$ and $\theta = \pi$.

$J \neq 0$) at g_1 = 4.5 MHz and ω_1 = 65 MHz. In the coupling regime of ($g_2 = 0$, $J = 0$), the probe absorption shows symmetrical splitting, as shown by the black curve in Figure 3A, which is analogous to EIT[67] in atomic systems because there is a transparent window (i.e., zero absorption deep) at $\Delta_s = 0$. A transparent window refers to transparent transmission without any absorption, and it is also termed phonon-induced transparency (PIT),[50] which is generated by mechanically induced coherent population oscillations when the condition of $\delta = \omega_1$ is met.[79,80] The physical origin of coherent population oscillation is that, when the pump and probe lasers with slightly different frequencies interact inside a saturable absorbing material, the atomic population is driven coherently between the ground and excited states at the beat frequency of the light beams.[79,80] For example, if a pump field at frequency ω and a detuned probe field at frequency $\omega + \delta$ co-propagate through a absorber, the ground state population will be induced to oscillate at frequency δ.[79,80] The single EIT-like window at $\Delta_s = 0$ in Figure 3A (the black line) is very similar to a single optomechanically induced transparency in a standard cavity optomechanical system formed by an optical cavity and a mechanical mode, which is due to the destructive interference of the probe field and the anti-Stokes scattering stimulated by the red-sideband driving.[81–84] In the coupling regime of ($g_2 \neq 0$, $J = 0$), that is, another CNT resonator is also introduced without considering the phonon-phonon coupling of the two CNT resonators, the probe absorption is supposed to present two EIT-like windows because there exist two routes of destructive interferences. However, we only obtain the counterintuitive phenomenon, that is, only one EIT-like window appears in the probe absorption [see the red dash line in Figure 3A], which is demonstrated that the bright mode plays an effective role in the destructive interference and the dark mode is decoupled in optomechanical system.[85] Compared with the coupling regime of ($g_2 = 0$, $J = 0$), the EIT-like window is amplified in the two-mechanical-mode CNT resonator system. If the coupling regime becomes ($g_2 \neq 0$, $J \neq 0$), we can observe that the probe absorption presents a analogous two-color EIT[68] with two symmetric splitting modes, that is, a single EIT-like window is divided into two symmetrical narrow EIT-like windows, as shown by the blue dot line in Figure 3A, where two zero-absorption deeps (transparent windows) located at $\Delta_s = \omega_1 - \Delta_p \pm J$ appear in the probe absorption. Actually, those features could be traced to coherent population oscillation. However, those coherent population oscillations are not just caused by pump and probe field, the external CNT resonator also make a contribution. Due to we consider the NV spin is a TLS, the spin-resonator coupling gets those two energy levels dressed with the vibration mode and those two energy levels should then be treated as two bands. If the affection from other resonators has been ignored, the coherent population oscillation caused by pump and probe field will result in a variation of the population distribution of those two bands and the coherent optical responses of the NV spin will also be changed. Those coherent population oscillations originate from the interband transitions caused by absorption and emission of photons. However, when the other CNT resonator is counted, the coherent population oscillations have different mechanism. The other CNT resonator acts as a "light beam", which directly drives intraband levels. The intraband transitions efficiently modify

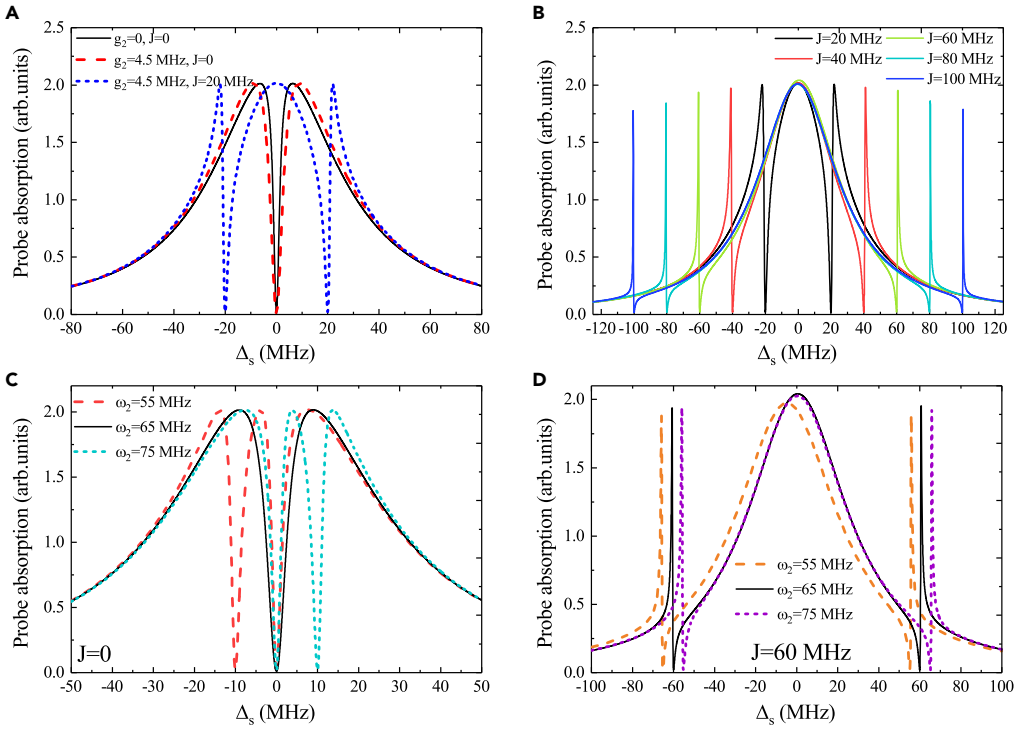

Figure 3. The probe absorption for different coupling regimes in the case of $\Delta_p \neq 0$

(A) The probe absorption for three coupling regimes of ($g_2 = 0$, $J = 0$), ($g_2 \neq 0$, $J = 0$), and ($g_2 \neq 0$, $J \neq 0$).

(B) The probe absorption spectra for different J.

(C) The probe absorption for different CNT resonators at $J = 0$.

(D) The probe absorption for different CNT resonators at $J = 60$ MHz.

the population distribution of those two bands and the optical responses of the NV spin. So the coherent population oscillation is assisted by the other CNT resonator, we refer to it as phonon assist-coherent population oscillation. Figure 3B further plots the probe absorption for different phonon-phonon coupling strengths J in the parametric regimes of $\omega_1 = \omega_2$, $g_1 = g_2$, and $\theta = \pi/2$. With increasing coupling strength J, the splitting width of the two absorption peaks is enhanced, and the splitting of the two absorption peaks is equal to the splitting width $2J$ which results from the Jaynes-Cummings coupling of the two CNT resonators.

On the other hand, two-color EIT effect was also demonstrated in a hybrid coupled system consisting of a single superconducting quantum circuit and a single NR, where the superconducting qubit is longitudinally coupled to the NR via an external flux,[86] rather than via the transverse coupling.[87] Compared with the transverse coupling, the longitudinal coupling has several advantages[86]: (1) There is no Purcell decay and residual interactions between a qubit and its resonator; (2) The parametrically modulated longitudinal coupling can be modulated in time at certain frequencies rather than always being a constant; (3) Even modulating the longitudinal coupling of two remote qubits and a resonator, a highfidelity controlled-phase gate can still be obtained. Therefore, the modulated longitudinal coupling offers another way to achieve better quantum control and engineering. In our hybrid quantum system, the coupling of NV spins between mechanical resonators is due to external magnetic field gradients,[4,11–14,17,30,31] where a magnetic tip is installed on a cantilever, generating magnetic coupling between the NV spin and NR. Compared with the work in ref.[86] which includes a single superconducting qubit coupled to a single NR, here we consider that an NV spin is coupled to two CNT resonators simultaneously. Further, we and ref.[86] both investigated the same optical response of two-color EIT in two different hybrid quantum systems by the modulated coupling with different forms, that is, the phase modulation of phonon-phonon interaction in our work and the amplitude modulation of spin-phonon coupling in ref.[86] Moreover, both the two hybrid quantum systems own the same advantages, i.e., they have the ability to interface hybrid material platforms to enhance light-matter interactions, which manifest a particularly promising integration platform and will lead to potential application in quantum information processing.[1,2,25]

Figure 3C investigates two CNT resonators with different frequencies that influence probe absorption under the condition of $J = 0$. If the two CNT resonators have the same frequencies ($\omega_1 = \omega_2$), the probe absorption displays standard single-color EIT at $\Delta_s = 0$ as shown the black curve in Figure 3C, which has been demonstrated in Figure 3A. However, if $\omega_2 < \omega_1$ ($\omega_1 = 65$ MHz and $\omega_2 = 55$ MHz), the probe absorption indicates a two-color EIT, as shown by the red curve in Figure 3C, and the two transparent windows are located at $\Delta_s = \omega_2 - \Delta_p$ ($\Delta_s = -10$ MHz) and $\Delta_s = \omega_1 - \Delta_p$ ($\Delta_s = 0$), respectively. If $\omega_2 > \omega_1$ ($\omega_1 = 65$ MHz and $\omega_2 = 75$ MHz), the probe absorption also manifests a two-color EIT, as shown by the green curve in Figure 3C, whereas the two transparent windows are located at $\Delta_s = \omega_1 - \Delta_p$ ($\Delta_s = 0$) and

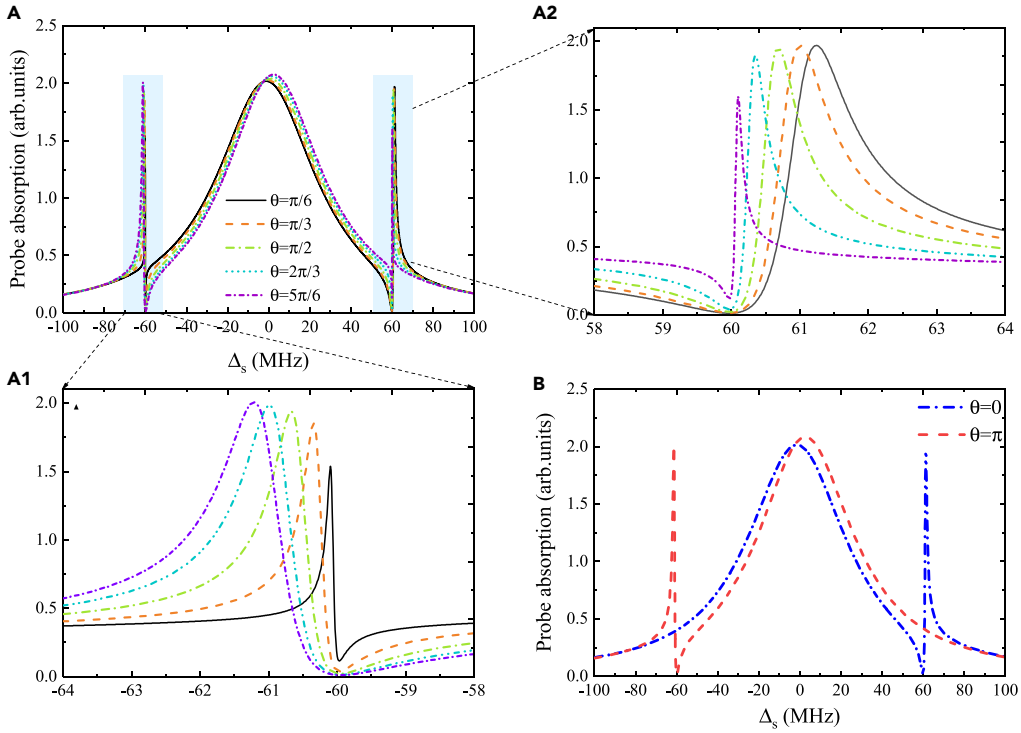

Figure 4. The probe absorption for different phase θ

(A) The probe absorption for five different phases θ. (A1) and (A2) The amplifying details in (A).

(B) The probe absorption for the phase $\theta = 0$ and $\theta = \pi$. The other parameters are $\Delta_p = \omega_1$, $\omega_1 = \omega_2$, $g_1 = g_2$, and $J = 60$ MHz.

$\Delta_s = \omega_2 - \Delta_p$ ($\Delta_s = 10$ MHz), respectively. We also further studied two different CNT resonators that affect the probe absorption under the condition of $J \neq 0$ (such as $J = 60$ MHz), as shown in Figure 3D. It is clear that the probe absorption presents a two-color EIT, and the two transparent windows are located at $\Delta_s = \overline{\omega} - \Delta_p \pm J$ with $\overline{\omega} = (\omega_1 + \omega_2)/2$. For example, if $\omega_1 = 65$ MHz and $\omega_2 = 55$ MHz, the two transparent windows are located at $\Delta_s = \overline{\omega} - \Delta_p - J = -65$ MHz and $\Delta_s = \overline{\omega} - \Delta_p + J = 55$ MHz with $\overline{\omega} = 60$ MHz, respectively. However, if $\omega_1 = 65$ MHz and $\omega_2 = 75$ MHz, the two transparent windows are located at $\Delta_s = \overline{\omega} - \Delta_p - J = -55$ MHz and $\Delta_s = \overline{\omega} - \Delta_p + J = 65$ MHz with $\overline{\omega} = 70$ MHz, respectively.

In addition, the modulation phase θ of the phonon-phonon coupling influences the two-color EIT was also investigated, as shown in Figure 4, which shows the probe absorption versus Δ_s for several different θ values in the parametric regime of $\omega_1 = \omega_2$, $g_1 = g_2$, and $J = 60$ MHz. The probe absorption presents a two-color EIT and two transparent windows located at $\Delta_s = \omega_1 - \Delta_p - J$ and $\Delta_s = \omega_1 - \Delta_p + J$, respectively. Figures 4A1 and 4A2 show the details of the left and right absorption peaks, which all manifest Fano-like resonances. The difference is that the spectral linewidth of the left Fano-like resonance is widened with the increase in intensity, while the spectral linewidth of the right Fano-like resonance is squeezed, accompanied by a decrease in intensity with increasing modulation phase θ from $\theta = \pi/6$ to $\theta = 5\pi/6$. In particular, the modulation phases $\theta = 0$ and $\theta = \pi$ are two special cases, in which the two-color EIT changes into the single-color EIT as shown in Figure 4B. If $\theta = 0$, then the single-color EIT window appears at $\Delta_s = \omega_1 - \Delta_p + J$, whereas if $\theta = \pi$, the single-color EIT window appears at $\Delta_s = \omega_1 - \Delta_p - J$. Combining the results in Figure 2B, where the left Fano-like resonance disappears and only leaves the right Fano resonance located at $\Delta_s = \omega_1 + J$ in the condition of $\theta = 0$; If $\theta = \pi$, the right Fano resonance disappears and the left Fano resonance located at $\Delta_s = \omega_1 - J$ moves to the left leading to the broad absorption peak located at $\Delta_s = 0$, which present the mode splitting phenomenon. The phenomena can be interpreted by the dark-mode effects, where the spin mode decouples from one of the two hybrid mechanical modes $\tilde{A}_+$ and $\tilde{A}_-$ (supplemental information of Section V). When $\theta = n\pi$ for an integer n, the spin mode is decoupled from one of the two hybridized mechanical modes $\tilde{A}_-$ (for an even number n) and $\tilde{A}_+$ (for an odd number n). So only the left or right Fano resonance appear in the probe absorption. In the case of the phase $\theta \neq n\pi$, the dark-mode effect can be broken by tuning the modulation phase, as a result both the right and left Fano resonance emerge in the probe absorption.

Moreover, the detuning Δ_p that dominates the probe absorption is also studied, as shown in Figure 5, with the parameters of $\omega_1 = \omega_2$, $g_1 = g_2$, $J = 60$ MHz, and $\theta = \pi/2$, Figures 5A1 and 5A2 show the details of the left and right Fano-like resonance peaks. With increasing detuning Δ_p from $\Delta_p = 0.8\omega_1$ to $\Delta_p = 1.2\omega_1$, we can obtain the following results: (1) The central broader absorption peaks around $\Delta_s = 0$ move from left to right with unchanged spectral linewidth in the probe absorption; (2) The spectral linewidth of the left Fano-like resonance is widened, while the right Fano-like resonance is squeezed; (3) The probe absorption presents a two-color EIT with two transparent windows located at $\Delta_s = \omega_1 - \Delta_p - J$ and $\Delta_s = \omega_1 - \Delta_p + J$, respectively.

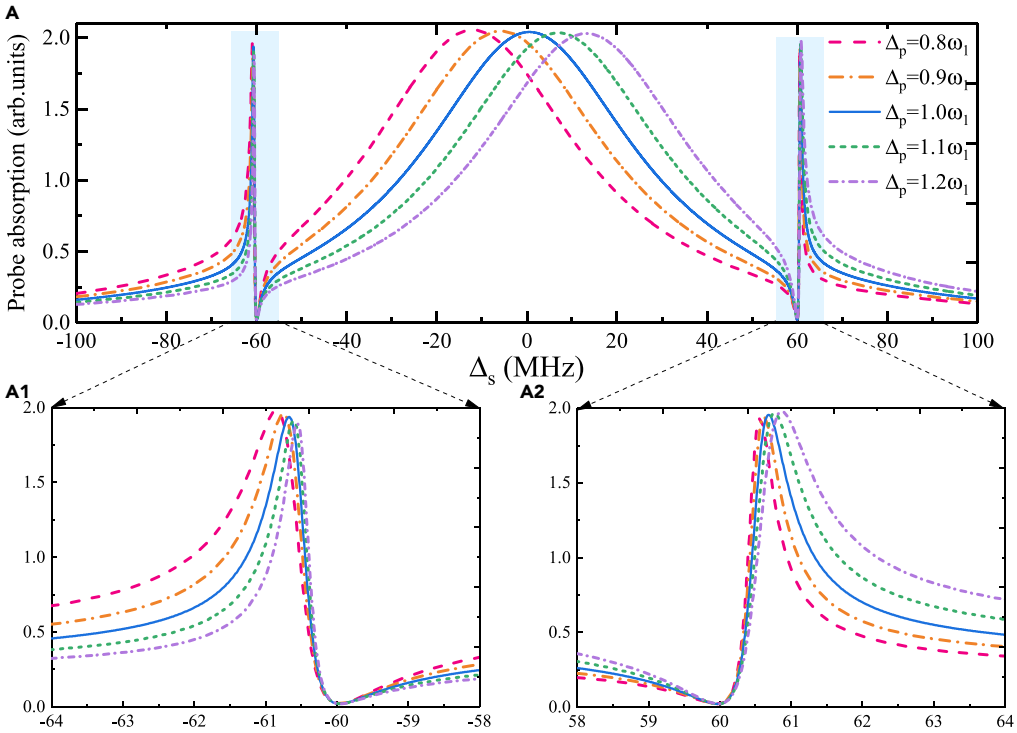

Figure 5. The probe absorption for different detuning Δ_p

(A) The probe absorption for five different detuning Δ_p. (A1) and (A2) The amplifying parts of the left and right peaks in (A). The other parameters are $\Delta_p = \omega_1$, $\omega_1 = \omega_2$, $g_1 = g_2$, $J = 60$ MHz, and $\theta = \pi/2$.

Both the single EIT and two-color EIT with transparent window (i.e., zero absorption deep) accompanied by rapid normal dispersion will lead to a subtle advancement or delay in light propagation. As demonstrated in ref. 79,80, a dispersion with a steep positive slope leads to a group velocity index $n_g > 0$, i.e., light delay (or slow light), whereas the dispersion with a steep negative slope generated a group velocity index of $n_g < 0$; i.e., light advances (or fast light). So the group velocity index n_g under different parametric regimes will be demonstrated in the following.

Figures 6 and 7 show the group velocity index n_g for different parametric regimes, which corresponds to the results in Figure 3. Figure 6A shows the middle peaks in Figure 3A that influences the index n_g in the parametric regimes of ($g_2 = 0, J = 0$) and ($g_2 = 4.5$ MHz, $J = 0$), and we can see that n_g experiences the process from $n_g > 0$ to $n_g < 0$, i.e., the transition from the slow light to fast light. In Figure 6B, the left and right absorption peaks (EIT windows) in Figure 3A inducing the slow and fast light are also demonstrated in the parametric regimes of ($g_2 =$ 4.5 MHz, $J = 20$ MHz), and it is obvious that the index n_g shows the change from slow to fast light. The difference is that the right peak in Figure 3A, which generates fast and slow light effects, is more significant than the left peak. Figures 6C and 6D correspond to the two-color EIT in Figure 3B, that is, the left and right Fano-like resonance that induces slow light with increasing coupling strength J from $J = 20$ MHz to $J = 100$ MHz with $\omega_1 = \omega_2$, $g_1 = g_2$, and $\theta = \pi/2$. In Figure 6C, if the coupling strength is small (e.g., $J \leq 40$ MHz), the index n_g manifests the conversion from slow to fast light, and when J reaches a critical value ($J > 60$ MHz), the slow light is dominant. The right Fano-like peak that affects the index n_g is shown in Figure 6D, where the change from slow to fast can be obtained, and the transition process is enhanced by increasing the coupling strength J.

Figure 7A corresponds to the middle EIT window in Figure 3C for different frequencies of CNT resonators without considering the phonon-phonon coupling ($J = 0$). If two CNT resonators have different frequencies (such as $\omega_2 > \omega_1$ or $\omega_2 < \omega_1$), they have the same group velocity index n_g, whereas if $\omega_2 = \omega_1$, the index n_g is smaller than that in the case of different frequencies. Figure 7B presents the left and right EIT windows in Figure 3C for $\omega_2 = 55$ MHz and $\omega_2 = 75$ MHz, respectively, which generate the group velocity, and the right EIT windows generate the group velocity that is more remarkable than the left one. If the coupling strength J is considered, the probe absorption displays a two-color EIT, as shown in Figure 3D. Figures 7C and 7D investigate the left and right peaks of the two-color EIT that generates the group velocity for different CNT resonators. Figure 7C plots the index n_g versus Rabi frequency Ω_p for three different CNT frequencies, and we find that if $\omega_2 \leq \omega_1$, the group velocity manifests as slow light; if $\omega_2 > \omega_1$, the group velocity experiences the process from slow to fast light. However, the right peak of the two-color EIT in Figure 3D, which induces the group velocity, as demonstrated in Figure 7D is quite different from the left one as shown in Figure 7C. If $\omega_2 < \omega_1$, the group velocity only indicates slow light, whereas if $\omega_2 \geq \omega_1$, the group velocity first arrives at a maximum value, then reduces to a minimum value, and finally reaches saturation with increasing Ω_p.

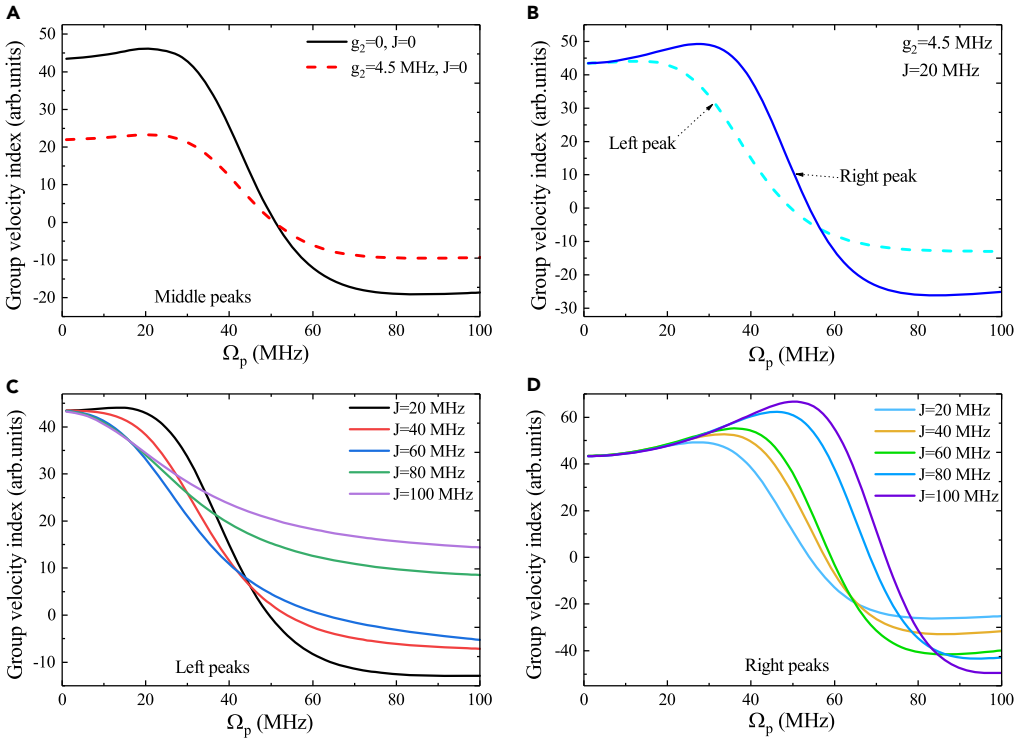

Figure 6. The group velocity index n_g for different coupling regimes

(A) The group velocity index n_g with respect to Ω_p in the parametric of ($g_2 = 0, J = 0$) and ($g_2 = 4.5$ MHz, $J = 0$) corresponding to the middle peaks in Figure 3A.

(B) The index n_g in the parameters of ($g_2 = 4.5$ MHz, $J = 20$ MHz) corresponding the left and right absorption peaks in Figure 3A.

(C) and (D) The index n_g for different J corresponding to the left and right peaks of two-color EIT in Figure 3B in the parameters of $\omega_1 = \omega_2$, $g_1 = g_2$, and $\theta = \pi/2$.

Figure 8 shows the modulation phase θ of the phonon-phonon coupling that influences the group velocity index n_g is demonstrated, which corresponds to the two-color EIT in Figure 4. Figure 8A plots the index n_g as a function of Ω_p for different phases θ with the parameters of $\omega_1 = \omega_2$, $g_1 = g_2$, and $J = 60$ MHz, which corresponds to the left peak of the two-color EIT in Figure 4A. The group velocity indicates slow light and gradually decreases from the maximum value for a fixed phase θ. Figure 8B gives the index n_g versus Ω_p for the same parameters in Figure 8A, which corresponds to the right peak of the two-color EIT in Figure 4A. Slow-to-fast light can be obtained, and when the phase θ reaches to $\theta = 5\pi/6$, the slow-to-fast light became more prominent. Moreover, we also plot the group velocity index n_g versus the modulation phase θ for different Ω_p values, as shown in Figures 8C and 8D, which correspond to the left and right peaks of the two-color EIT in Figure 4A. The slow-to-fast and fast-to-slow light effects can be generated in the two-color EIT windows by controlling the modulation phase θ. For the left peaks of the two-color EIT induced optical propagation, as shown in Figure 8C, the group velocity indicates the fast-to-slow light appearing in $\theta \in [0, \pi]$ and the slow-to-fast light effect emerges at $\theta \in [\pi, 2\pi]$. For the right peaks, as shown in Figure 8D, the slow-to-fast and fast-to-slow light effects change tempestuously at approximately $\theta = \pi$.

Figure 9 shows the detuning Δ_p that affects the group velocity, which corresponds to the two-color EIT in Figure 5. Figure 9A shows the index n_g versus Ω_p for different detuning Δ_p with the parameters of $\omega_1 = \omega_2$, $g_1 = g_2$, $J = 60$ MHz, and $\theta = \pi/2$, which corresponds to the left peak of the two-color EIT in Figure 5, and the slow-light effect decreases gradually from the same maximum value for different Δ_p. The group velocity index n_g versus the phase θ for different Δ_p is demonstrated in Figure 9B, which corresponds to the left peak of the two-color EIT in Figure 5, and the results are similar to the results in Figure 8C. Figure 9C plots the index n_g versus Ω_p for different detuning Δ_p with the same parameters as in Figure 9A, which corresponds to the right peak of the two-color EIT in Figure 5, and the slow-to-fast light effect can be obtained. Figure 9D displays the group velocity index n_g versus the phase θ for different Δ_p, which corresponds to the right peak of the two-color EIT Figure 5, and the results are similar to the results in Figure 8D, i.e., the slow-to-fast and fast-to-slow light effects happen around $\theta = \pi$. These results can result in ultraslowing or ultra-advancing signals that can be applied to optical storage or quantum communication.[82,83]

DISCUSSIONS

We have studied probe absorption in a multiple-mode-coupling hybrid quantum system, which consists of two-mode-coupling nanomechanical CNT resonators coupled to the same NV center in diamond. In this system, the NV center is considered a two-level system, which can be

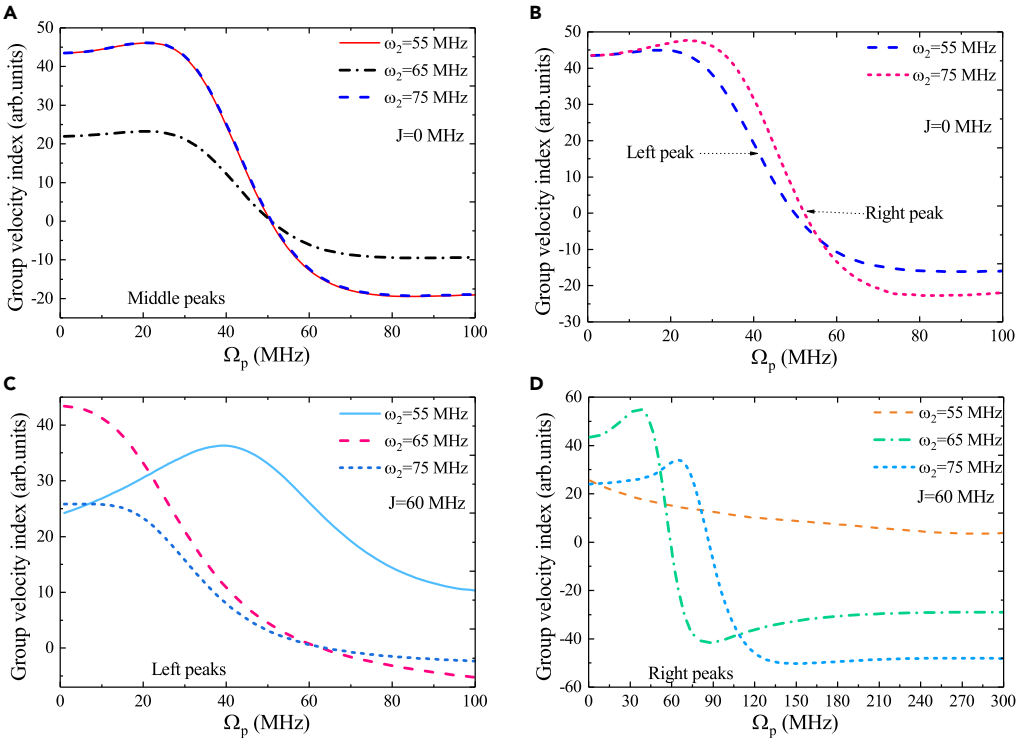

Figure 7. The group velocity index n_g for different frequencies

(A) The index n_g for different frequencies of CNT resonators at . corresponding to the middle EIT window in Figure 3C.

(B) The index n_g for ω_2 = 55 MHz and ω_2 = 75 MHz at J = 0 corresponding to the left and right EIT windows in Figure 3C.

(C) The index n_g versus Ω_p for three different CNT frequencies corresponding to the left peak of two-color EIT in Figure 3D.

(D) The index n_g for different CNT frequencies corresponding to the right peak of two-color EIT in Figure 3D.

replaced by superconducting qubits, atoms, or quantum dots, while the two-mode-coupling CNT resonators can also be replaced by doubly clamped nanomechanical resonators, cantilever resonators, or two-dimensional drum resonators. The interactions of NV spins and mechanical resonators can be achieved by magnetomechanical interactions or strain-mediated coupling, and the two CNT resonators couple with each other via phase-dependent phonon-exchange coupling.

We have investigated the optical responses of the NV spin in diamond, and the probe absorption shows two transparent windows, which is called a two-color EIT, in contrast to the standard single-color EIT. The switch between one and two EIT windows can be controlled periodically by manipulating the modulation phase of the phonon-phonon coupling. Combining the coupling of NV spin and CNT resonators with phonon-phonon coupling, two-color EIT windows that generate light delay or advance have been demonstrated, and by periodically tuning the modulation phase, the switch of slow-to-fast and fast-to-slow light effects can be achieved. This study present a promising integration platform for chip-scale applications in information processing.

Limitations of the study

In this study, we designed a multiple-mode-coupling hybrid quantum system to investigate the slow light effect by periodically tuning the modulation phase. However, experimental implementation of the scheme still requires advances in micro(nano) science and technology.

STAR★METHODS

Detailed methods are provided in the online version of this paper and include the following:

- KEY RESOURCES TABLE
- RESOURCE AVAILABILITY
  - Lead contact
  - Materials availability
  - Data and code availability
- METHOD DETAILS
  - Model and Hamiltonian

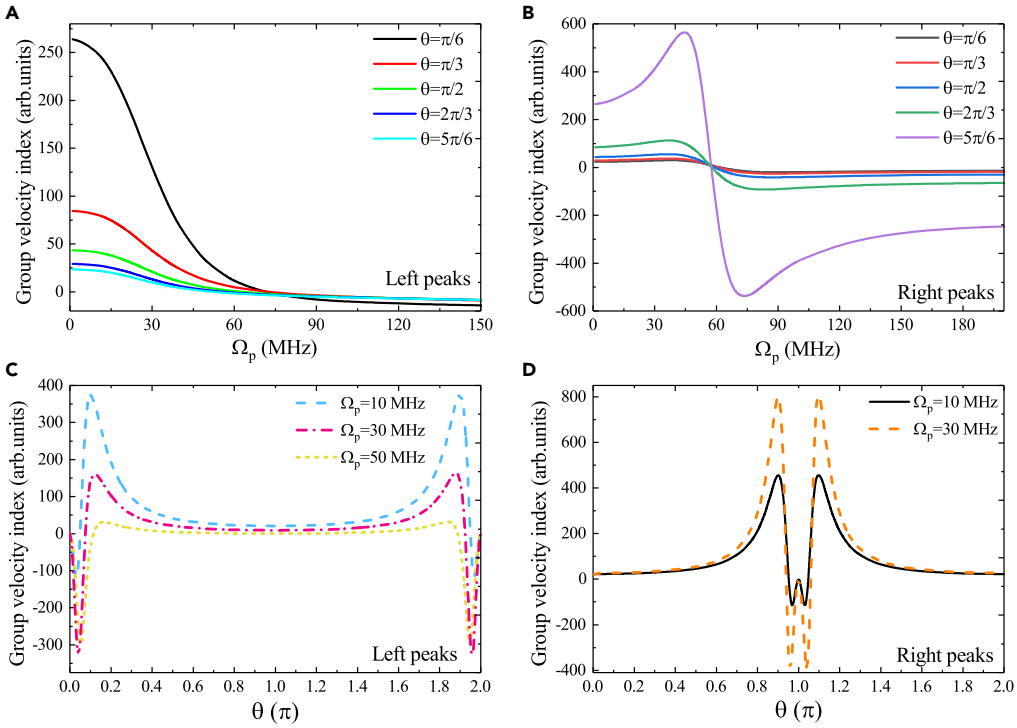

Figure 8. The group velocity index n_g for different Ω_p and θ

(A) The index n_g versus Ω_p for different phase θ with the parameters of $\omega_1 = \omega_2$, $g_1 = g_2$, and J = 60 MHz corresponding to the left peak of the two-color EIT Figure 4A.

(B) The index n_g for the same parameters in (A) corresponding to the right peak of the two-color EIT Figure 4A.

(C) and (D) The group velocity index n_g versus the phase θ for different Ω_p corresponding to the left and right peak of the two-color EIT in Figure 4A.

- Heisenberg-Langevin equations
- Linear optical susceptibility
- Dark-mode effect
- The light group velocity

- QUANTIFICATION AND STATISTICAL ANALYSIS

SUPPLEMENTAL INFORMATION

Supplemental information can be found online at https://doi.org/10.1016/j.isci.2024.109328.

ACKNOWLEDGMENTS

H.-J.C. acknowledges the support from the National Natural Science Foundation of China under Grant No.11804004 and No.11647001. This work is also supported by the China Postdoctoral Science Foundation under Grant No.2020M681973.

AUTHOR CONTRIBUTIONS

H.-J.C. provided the ideas, performed the numerical calculations and analyzed the data, prepared the figures, wrote the manuscript, and supervised the work.

DECLARATION OF INTERESTS

The authors declare no competing interests.

Received: October 25, 2023
Revised: January 3, 2024
Accepted: February 20, 2024
Published: February 28, 2024

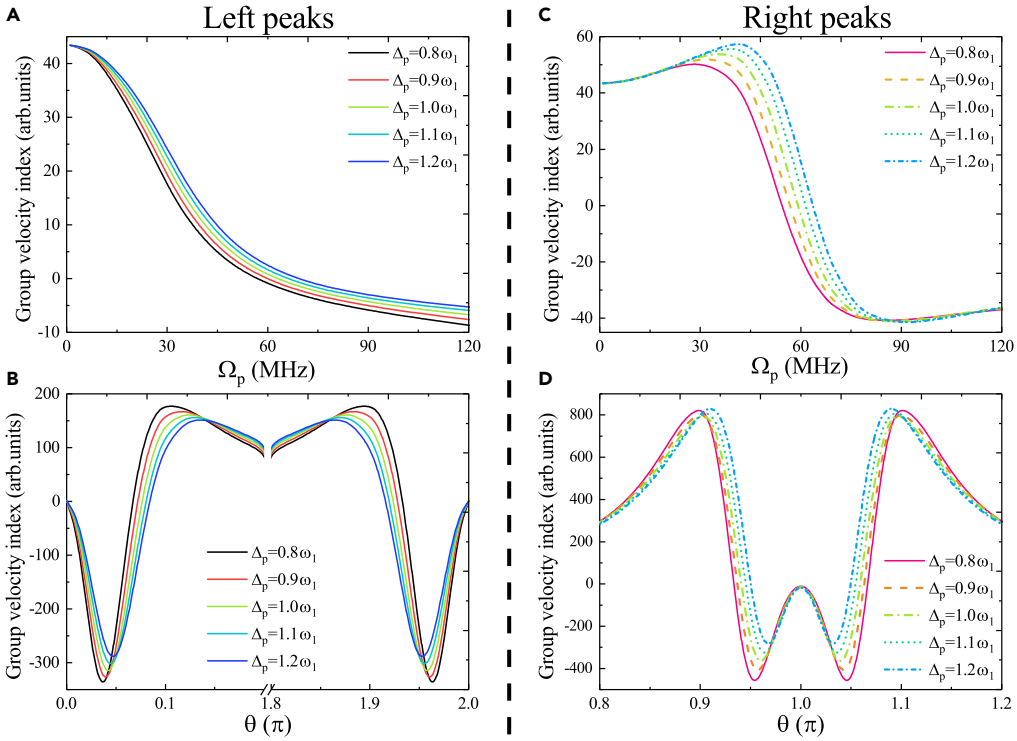

Figure 9. The group velocity index n_g for different detuning Δ_p

(A) The index n_g versus Ω_p for different detuning Δ_p in the parameters of $\omega_1 = \omega_2$, $g_1 = g_2$, $J = 60$ MHz, and $\theta = \pi/2$ corresponding to the left peak of the two-color EIT Figure 5.

(B) The index n_g for the same parameters in (A) corresponding to the right peak of the two-color EIT Figure 5.

(C) and (D) The index n_g versus Ω_p for different detuning Δ_p corresponding to the left and right peak of the two-color EIT in Figure 5.

REFERENCES

1. Xiang, Z.L., Ashhab, S., You, J.Q., and Nori, F. (2013). Hybrid quantum circuits: Superconducting circuits interacting with other quantum systems. Rev. Mod. Phys. *85*, 623.
2. Kurizki, G., Bertet, P., Kubo, Y., MØlmer, K., Petrosyan, D., Rabl, P., and Schmiedmayer, J. (2015). Quantum technologies with hybrid systems. Proc. Natl Acad. Sci. USA *112*, 3866–3873.
3. Etaki, S., Poot, M., Mahboob, I., Onomitsu, K., Yamaguchi, H., and Van der Zant, H.S.J. (2008). Motion detection of a micromechanical resonator embedded in a dc SQUID. Nat. Phys. *4*, 785–788.
4. Arcizet, O., Jacques, V., Siria, A., Poncharal, P., Vincent, P., and Seidelin, S. (2011). A single nitrogen-vacancy defect coupled to a nanomechanical oscillator. Nat. Phys. *7*, 879–883.
5. Jöckel, A., Faber, A., Kampschulte, T., Korppi, M., Rakher, M.T., and Treutlein, P. (2015). Sympathetic cooling of a membrane oscillator in a hybrid mechanical–atomic system. Nat. Nanotechnol. *10*, 55–59.
6. Yeo, I., de Assis, P.L., Gloppe, A., Dupont-Ferrier, E., Verlot, P., Malik, N.S., Dupuy, E., Claudon, J., Gérard, J.M., Auffèves, A., et al. (2014). Strain-mediated coupling in a quantum dot–mechanical oscillator hybrid system. Nat. Nanotechnol. *9*, 106–110.
7. Montinaro, M., Wüst, G., Munsch, M., Fontana, Y., Russo-Averchi, E., Heiss, M., Fontcuberta I Morral, A., Warburton, R.J., and Poggio, M. (2014). Quantum dot opto-mechanics in a fully self-assembled nanowire. Nano Lett. *14*, 4454–4460.
8. Yao, N.Y., Jiang, L., Gorshkov, A.V., Maurer, P.C., Giedke, G., Cirac, J.I., and Lukin, M.D. (2012). Scalable architecture for a room temperature solid-state quantum information processor. Nat. Commun. *3*, 800.
9. Dolde, F., Jakobi, I., Naydenov, B., Zhao, N., Pezzagna, S., Trautmann, C., Meijer, J., Neumann, P., Jelezko, F., and Wrachtrup, J. (2013). Room-temperature entanglement between single defect spins in diamond. Nat. Phys. *9*, 139–143.
10. Cai, J., Retzker, A., Jelezko, F., and Plenio, M.B. (2013). A large-scale quantum simulator on a diamond surface at room temperature. Nat. Phys. *9*, 168–173.
11. Li, P.B., and Nori, F. (2018). Hybrid quantum system with nitrogen-vacancy centers in diamond coupled to surface-phonon polaritons in piezomagnetic superlattices. Phys. Rev. Appl. *10*, 024011.
12. Li, B., Li, P.B., Zhou, Y., Liu, J., Li, H.R., and Li, F.L. (2019). Interfacing a topological qubit with a spin qubit in a hybrid quantum system. Phys. Rev. Appl. *11*, 044026.
13. Rabl, P., Cappellaro, P., Dutt, M.V.G., Jiang, L., Maze, J.R., and Lukin, M.D. (2009). Strong magnetic coupling between an electronic spin qubit and a mechanical resonator. Phys. Rev. B *79*, 041302.
14. Rabl, P., Kolkowitz, S.J., Koppens, F.H.L., Harris, J.G.E., Zoller, P., and Lukin, M.D. (2010). A quantum spin transducer based on nanoelectromechanical resonator arrays. Nat. Phys. *6*, 602–608.
15. Kolkowitz, S., Jayich, A.C.B., Unterreithmeier, Q.P., Bennett, S.D., Rabl, P., Harris, J.G.E., and Lukin, M.D. (2012). Coherent sensing of a mechanical resonator with a single-spin qubit. Science *335*, 1603–1606.
16. Hong, S., Grinolds, M.S., Maletinsky, P., Walsworth, R.L., Lukin, M.D., and Yacoby, A. (2012). Coherent, mechanical control of a single electronic spin. Nano Lett. *12*, 3920–3924.
17. MacQuarrie, E.R., Gosavi, T.A., Jungwirth, N.R., Bhave, S.A., and Fuchs, G.D. (2013). Mechanical spin control of nitrogen-vacancy centers in diamond. Phys. Rev. Lett. *111*, 227602.
18. Teissier, J., Barfuss, A., Appel, P., Neu, E., and Maletinsky, P. (2014). Strain coupling of a nitrogen-vacancy center spin to a diamond mechanical oscillator. Phys. Rev. Lett. *113*, 020503.
19. Poot, M., and van der Zant, H.S. (2012). Mechanical systems in the quantum regime. Phys. Rep. *511*, 273–335.

20. Degen, C., Reinhard, F., and Cappellaro, P. (2017). Quantum sensing. Rev. Mod. Phys. *89*, 035002.
21. Xu, B., Zhang, P., Zhu, J., Liu, Z., Eichler, A., Zheng, X.Q., Lee, J., Dash, A., More, S., Wu, S., et al. (2022). Nanomechanical resonators: toward atomic scale. ACS Nano *16*, 15545–15585.
22. Lassagne, B., Ugnati, D., and Respaud, M. (2011). Ultrasensitive magnetometers based on carbon-nanotube mechanical resonators. Phys. Rev. Lett. *107*, 130801.
23. Moser, J., Güttinger, J., Eichler, A., Esplandiu, M.J., Liu, D.E., Dykman, M.I., and Bachtold, A. (2013). Ultrasensitive force detection with a nanotube mechanical resonator. Nat. Nanotechnol. *8*, 493–496.
24. Tavernarakis, A., Stavrinadis, A., Nowak, A., Tsioutsios, I., Bachtold, A., and Verlot, P. (2018). Optomechanics with a hybrid carbon nanotube resonator. Nat. Commun. *9*, 662.
25. Bachtold, A., Moser, J., and Dykman, M. (2022). Mesoscopic physics of nanomechanical systems. Rev. Mod. Phys. *94*, 045005.
26. Maze, J.R., Gali, A., Togan, E., Chu, Y., Trifonov, A., Kaxiras, E., and Lukin, M.D. (2011). Properties of nitrogen-vacancy centers in diamond: the group theoretic approach. New J. Phys. *13*, 025025.
27. Cao, C., Duan, Y.W., Chen, X., Zhang, R., Wang, T.J., and Wang, C. (2017). Implementation of single-photon quantum routing and decoupling using a nitrogen-vacancy center and a whispering-gallery-mode resonator-waveguide system. Opt Express *25*, 16931–16946.
28. Lachance-Quirion, D., Tabuchi, Y., Gloppe, A., Usami, K., and Nakamura, Y. (2019). Hybrid quantum systems based on magnonics. APEX *12*, 070101.
29. Cao, C., Han, Y.H., Yi, X., Yin, P.P., Zhang, X.Y., Gao, Y.P., Fan, L., and Zhang, R. (2021). Implementation of a single-photon fully quantum router with cavity QED and linear optics. Opt. Quant. Electron. *53*, 32.
30. Bennett, S.D., Yao, N.Y., Otterbach, J., Zoller, P., Rabl, P., and Lukin, M.D. (2013). Phonon-induced spin-spin interactions in diamond nanostructures: application to spin squeezing. Phys. Rev. Lett. *110*, 156402.
31. Kepesidis, K.V., Bennett, S.D., Portolan, S., Lukin, M.D., and Rabl, P. (2013). Phonon cooling and lasing with nitrogen-vacancy centers in diamond. Phys. Rev. B *88*, 064105.
32. Chotorlishvili, L., Sander, D., Sukhov, A., Dugaev, V., Vieira, V.R., Komnik, A., and Berakdar, J. (2013). Entanglement between nitrogen vacancy spins in diamond controlled by a nanomechanical resonator. Phys. Rev. B *88*, 085201.
33. Ovartchaiyapong, P., Lee, K.W., Myers, B.A., and Jayich, A.C.B. (2014). Dynamic strain-mediated coupling of a single diamond spin to a mechanical resonator. Nat. Commun. *5*, 4429.
34. Pigeau, B., Rohr, S., Mercier de Lépinay, L., Gloppe, A., Jacques, V., and Arcizet, O. (2015). Observation of a phononic Mollow triplet in a multimode hybrid spin-nanomechanical system. Nat. Commun. *6*, 8603.
35. Meesala, S., Sohn, Y.I., Atikian, H.A., Kim, S., Burek, M.J., Choy, J.T., and Lončar, M. (2016). Enhanced strain coupling of nitrogen-vacancy spins to nanoscale diamond cantilevers. Phys. Rev. Appl. *5*, 034010.
36. Lee, K.W., Lee, D., Ovartchaiyapong, P., Minguzzi, J., Maze, J.R., and Bleszynski Jayich, A.C. (2016). Strain coupling of a mechanical resonator to a single quantum emitter in diamond. Phys. Rev. Appl. *6*, 034005.
37. MacQuarrie, E.R., Otten, M., Gray, S.K., and Fuchs, G.D. (2017). Cooling a mechanical resonator with nitrogen-vacancy centres using a room temperature excited state spin–strain interaction. Nat. Commun. *8*, 14358.
38. Li, P.B., Zhou, Y., Gao, W.B., and Nori, F. (2020). Enhancing spin-phonon and spin-spin interactions using linear resources in a hybrid quantum system. Phys. Rev. Lett. *125*, 153602.
39. Li, P.B., Xiang, Z.L., Rabl, P., and Nori, F. (2016). Hybrid quantum device with nitrogen-vacancy centers in diamond coupled to carbon nanotubes. Phys. Rev. Lett. *117*, 015502.
40. Li, S.X., Zhu, D., Wang, X.H., Wang, J.T., Deng, G.W., Li, H.O., Cao, G., Xiao, M., Guo, G.C., Jiang, K.L., et al. (2016). Parametric strong mode-coupling in carbon nanotube mechanical resonators. Nanoscale *8*, 14809–14813.
41. De Alba, R., Massel, F., Storch, I.R., Abhilash, T.S., Hui, A., McEuen, P.L., Craighead, H.G., and Parpia, J.M. (2016). Tunable phonon-cavity coupling in graphene membranes. Nat. Nanotechnol. *11*, 741–746.
42. Güttinger, J., Noury, A., Weber, P., Eriksson, A.M., Lagoin, C., Moser, J., Eichler, C., Wallraff, A., Isacsson, A., and Bachtold, A. (2017). Energy-dependent path of dissipation in nanomechanical resonators. Nat. Nanotechnol. *12*, 631–636.
43. Cho, S., Cho, S.U., Jo, M., Suh, J., Park, H.C., Kim, S.G., Shim, S.B., and Park, Y.D. (2018). Strong two-mode parametric interaction and amplification in a nanomechanical resonator. Phys. Rev. Appl. *9*, 064023.
44. Prasad, P., Arora, N., and Naik, A.K. (2019). Gate tunable cooperativity between vibrational modes. Nano Lett. *19*, 5862–5867.
45. Faust, T., Rieger, J., Seitner, M.J., Kotthaus, J.P., and Weig, E.M. (2013). Coherent control of a classical nanomechanical two-level system. Nat. Phys. *9*, 485–488.
46. Castellanos-Gomez, A., Meerwaldt, H.B., Venstra, W.J., van der Zant, H.S.J., and Steele, G.A. (2012). Strong and tunable mode coupling in carbon nanotube resonators. Phys. Rev. B *86*, 041402.
47. Eichler, A., del Álamo Ruiz, M., Plaza, J.A., and Bachtold, A. (2012). Strong coupling between mechanical modes in a nanotube resonator. Phys. Rev. Lett. *109*, 025503.
48. Mathew, J.P., Patel, R.N., Borah, A., Vijay, R., and Deshmukh, M.M. (2016). Dynamical strong coupling and parametric amplification of mechanical modes of graphene drums. Nat. Nanotechnol. *11*, 747–751.
49. Zhu, D., Wang, X.H., Kong, W.C., Deng, G.W., Wang, J.T., Li, H.O., Cao, G., Xiao, M., Jiang, K.L., Dai, X.C., et al. (2017). Coherent phonon Rabi oscillations with a high-frequency carbon nanotube phonon cavity. Nano Lett. *17*, 915–921.
50. Okamoto, H., Gourgout, A., Chang, C.Y., Onomitsu, K., Mahboob, I., Chang, E.Y., and Yamaguchi, H. (2013). Coherent phonon manipulation in coupled mechanical resonators. Nat. Phys. *9*, 480–484.
51. Oeckinghaus, T., Momenzadeh, S.A., Scheiger, P., Shalomayeva, T., Finkler, A., Dasari, D., Stöhr, R., and Wrachtrup, J. (2020). Spin–phonon interfaces in coupled nanomechanical cantilevers. Nano Lett. *20*, 463–469.
52. Xu, X.W., Liu, Y.X., Sun, C.P., and Li, Y. (2015). Mechanical PT symmetry in coupled optomechanical systems. Phys. Rev. A *92*, 013852.
53. Chen, H.J. (2023). The fast–slow light transitions induced by Fano resonance in multiple nanomechanical resonators. Opt Laser. Technol. *161*, 109242.
54. Xu, X.W., and Li, Y. (2015). Optical nonreciprocity and optomechanical circulator in three-mode optomechanical systems. Phys. Rev. A *91*, 053854.
55. Jiao, Y., Lü, H., Qian, J., Li, Y., and Jing, H. (2016). Nonlinear optomechanics with gain and loss: amplifying higher-order sideband and group delay. New J. Phys. *18*, 083034.
56. Monifi, F., Zhang, J., Özdemir, Ş.K., Peng, B., Liu, Y.X., Bo, F., Nori, F., and Yang, L. (2016). Optomechanically induced stochastic resonance and chaos transfer between optical fields. Nat. Photonics *10*, 399–405.
57. Cao, C., Chen, X., Duan, Y.W., and Zhang, R. (2018). Photonic coherent perfect transmission, absorption, and synthesis in a bimodal cavity quantum electrodynamics system. Optik *161*, 293–300.
58. Chen, Y., Zhang, Y.L., Shen, Z., Zou, C.L., Guo, G.C., and Dong, C.H. (2021). Synthetic gauge fields in a single optomechanical resonator. Phys. Rev. Lett. *126*, 123603.
59. Zhang, X.Y., Cao, C., Gao, Y.P., Fan, L., Zhang, R., and Wang, C. (2023). Generation and manipulation of phonon lasering in a two-drive cavity magnomechanical system. New J. Phys. *25*, 053039.
60. Massel, F., Cho, S.U., Pirkkalainen, J.M., Hakonen, P.J., Heikkilä, T.T., and Sillanpää, M.A. (2012). Multimode circuit optomechanics near the quantum limit. Nat. Commun. *3*, 987.
61. Ma, P.C., Zhang, J.Q., Xiao, Y., Feng, M., and Zhang, Z.M. (2014). Tunable double optomechanically induced transparency in an optomechanical system. Phys. Rev. A *90*, 043825.
62. Childress, L., Gurudev Dutt, M.V., Taylor, J.M., Zibrov, A.S., Jelezko, F., Wrachtrup, J., Hemmer, P.R., and Lukin, M.D. (2006). Coherent dynamics of coupled electron and nuclear spin qubits in diamond. Science *314*, 281–285.
63. Gaebel, T., Domhan, M., Popa, I., Wittmann, C., Neumann, P., Jelezko, F., Rabeau, J.R., Stavrias, N., Greentree, A.D., Prawer, S., et al. (2006). Room-temperature coherent coupling of single spins in diamond. Nat. Phys. *2*, 408–413.
64. Hanson, R., and Awschalom, D.D. (2008). Coherent manipulation of single spins in semiconductors. Nature *453*, 1043–1049.
65. Fang, K., Luo, J., Metelmann, A., Matheny, M.H., Marquardt, F., Clerk, A.A., and Painter, O. (2017). Generalized non-reciprocity in an optomechanical circuit via synthetic magnetism and reservoir engineering. Nat. Phys. *13*, 465–471.
66. Wilson-Rae, I., Zoller, P., and Imamoğlu, A. (2004). Laser cooling of a nanomechanical resonator mode to its quantum ground state. Phys. Rev. Lett. *92*, 075507.
67. Fleischhauer, M., Imamoglu, A., and Marangos, J.P. (2005). Electromagnetically

induced transparency: Optics in coherent media. Rev. Mod. Phys. *77*, 633–673.
68. Wang, H., Gu, X., Liu, Y.X., Miranowicz, A., and Nori, F. (2014). Optomechanical analog of two-color electromagnetically induced transparency: Photon transmission through an optomechanical device with a two-level system. Phys. Rev. A *90*, 023817.
69. Verhagen, E., Deléglise, S., Weis, S., Schliesser, A., and Kippenberg, T.J. (2012). Quantum-coherent coupling of a mechanical oscillator to an optical cavity mode. Nature *482*, 63–67.
70. Lai, D.G., Zou, F., Hou, B.P., Xiao, Y.F., and Liao, J.Q. (2018). Simultaneous cooling of coupled mechanical resonators in cavity optomechanics. Phys. Rev. A *98*, 023860.
71. Liao, Q., Qiu, H., Xiao, M., and Nie, W. (2023). Probe absorption characteristics and a tunable susceptibility switch of a superconducting flux qubit coupled to two mechanical resonators. Opt Laser. Technol. *159*, 108992.
72. Song, X., Oksanen, M., Li, J., Hakonen, P.J., and Sillanpää, M.A. (2014). Graphene optomechanics realized at microwave frequencies. Phys. Rev. Lett. *113*, 027404.
73. Singh, V., Bosman, S.J., Schneider, B.H., Blanter, Y.M., Castellanos-Gomez, A., and Steele, G.A. (2014). Optomechanical coupling between a multilayer graphene mechanical resonator and a superconducting microwave cavity. Nat. Nanotechnol. *9*, 820–824.
74. Fano, U. (1961). Effects of configuration interaction on intensities and phase shifts. Phys. Rev. *124*, 1866–1878.
75. Wu, C., Khanikaev, A.B., Adato, R., Arju, N., Yanik, A.A., Altug, H., and Shvets, G. (2011). Fano-resonant asymmetric metamaterials for ultrasensitive spectroscopy and identification of molecular monolayers. Nat. Mater. *11*, 69–75.
76. Zhou, Z.K., Peng, X.N., Yang, Z.J., Zhang, Z.S., Li, M., Su, X.R., Zhang, Q., Shan, X., Wang, Q.Q., and Zhang, Z. (2011). Tuning gold nanorod-nanoparticle hybrids into plasmonic Fano resonance for dramatically enhanced light emission and transmission. Nano Lett. *11*, 49–55.
77. Taubert, R., Hentschel, M., Kästel, J., and Giessen, H. (2012). Classical analog of electromagnetically induced absorption in plasmonics. Nano Lett. *12*, 1367–1371.
78. Wu, C., Khanikaev, A.B., and Shvets, G. (2011). Broadband slow light metamaterial based on a double-continuum Fano resonance. Phys. Rev. Lett. *106*, 107403.
79. Boyd, R.W., and Gauthier, D.J. (2009). Controlling the velocity of light pulses. Science *326*, 1074–1077.
80. Boyd, R.W. (2009). Slow and fast light: fundamentals and applications. J. Mod. Opt. *56*, 1908–1915.
81. Agarwal, G.S., and Huang, S. (2010). Electromagnetically induced transparency in mechanical effects of light. Phys. Rev. A *81*, 041803.
82. Weis, S., Rivière, R., Deléglise, S., Gavartin, E., Arcizet, O., Schliesser, A., and Kippenberg, T.J. (2010). Optomechanically induced transparency. Science *330*, 1520–1523.
83. Safavi-Naeini, A.H., Mayer Alegre, T.P., Chan, J., Eichenfield, M., Winger, M., Lin, Q., Hill, J.T., Chang, D.E., and Painter, O. (2011). Electromagnetically induced transparency and slow light with optomechanics. Nature *472*, 69–73.
84. Teufel, J.D., Li, D., Allman, M.S., Cicak, K., Sirois, A.J., Whittaker, J.D., and Simmonds, R.W. (2011). Circuit cavity electromechanics in the strong-coupling regime. Nature *471*, 204–208.
85. Lai, D.G., Wang, X., Qin, W., Hou, B.P., Nori, F., and Liao, J.Q. (2020). Tunable optomechanically induced transparency by controlling the dark-mode effect. Phys. Rev. A *102*, 023707.
86. Wang, X., Miranowicz, A., Li, H.R., Li, F.L., and Nori, F. (2018). Two-color electromagnetically induced transparency via modulated coupling between a mechanical resonator and a qubit. Phys. Rev. A *98*, 023821.
87. Stassi, R., and Nori, F. (2018). Long-lasting quantum memories: Extending the coherence time of superconducting artificial atoms in the ultrastrong-coupling regime. Phys. Rev. A *97*, 033823.
88. Lai, D.G., Huang, J.F., Yin, X.L., Hou, B.P., Li, W., Vitali, D., Nori, F., and Liao, J.Q. (2020). Nonreciprocal ground-state cooling of multiple mechanical resonators. Phys. Rev. A *102*, 011502.
89. Lai, D.G., Liao, J.Q., Miranowicz, A., and Nori, F. (2022). Noise-tolerant optomechanical entanglement via synthetic magnetism. Phys. Rev. Lett. *129*, 063602.
90. Rong, X., Wang, M., Geng, J., Qin, X., Guo, M., Jiao, M., Xie, Y., Wang, P., Huang, P., Shi, F., et al. (2018). Searching for an exotic spin-dependent interaction with a single electron-spin quantum sensor. Nat. Commun. *9*, 739.
91. Massel, F., Heikkilä, T.T., Pirkkalainen, J.M., Cho, S.U., Saloniemi, H., Hakonen, P.J., and Sillanpää, M.A. (2011). Microwave amplification with nanomechanical resonators. Nature *480*, 351–354.
92. Fang, K., Matheny, M.H., Luan, X., and Painter, O. (2016). Optical transduction and routing of microwave phonons in cavity-optomechanical circuits. Nat. Photonics *10*, 489–496.
93. Hensinger, W.K., Utami, D.W., Goan, H.S., Schwab, K., Monroe, C., and Milburn, G.J. (2005). Ion trap transducers for quantum electromechanical oscillators. Phys. Rev. A *72*, 041405.
94. Wang, Q., Zhang, J.Q., Ma, P.C., Yao, C.M., and Feng, M. (2015). Precision measurement of the environmental temperature by tunable double optomechanically induced transparency with a squeezed field. Phys. Rev. A *91*, 063827.
95. Chen, H.J. (2021). Multiple-Fano-resonance-induced fast and slow light in the hybrid nanomechanical-resonator system. Phys. Rev. A *104*, 013708.
96. Liu, Y.X., You, J.Q., Wei, L.F., Sun, C.P., and Nori, F. (2005). Optical selection rules and phase-dependent adiabatic state control in a superconducting quantum circuit. Phys. Rev. Lett. *95*, 087001.
97. Tian, L., and Zoller, P. (2004). Coupled ion-nanomechanical systems. Phys. Rev. Lett. *93*, 266403.
98. Frisk Kockum, A., Miranowicz, A., De Liberato, S., Savasta, S., and Nori, F. (2019). Ultrastrong coupling between light and matter. Nat. Rev. Phys. *1*, 19–40.
99. Boyd, R.W. (1992). Nonlinear Optics (Academic), p. 225.
100. Walls, D.F., and Milburn, G.J. (1994). Quantum Optics (Springer), pp. 245–265.
101. Gardiner, C., and Zoller, P. (2000). Quantum Noise (Springer).
102. Chen, H.J. (2021). Controllable fast and slow light in the hybrid quantum dot–nanomechanical resonator system mediated by another nanomechanical resonator with Coulomb interaction. J. Appl. Phys. *130*, 204302.
103. Zhu, Z., Gauthier, D.J., and Boyd, R.W. (2007). Stored light in an optical fiber via stimulated Brillouin scattering. Science *318*, 1748–1750.

STAR★METHODS

KEY RESOURCES TABLE

REAGENT or RESOURCE	SOURCE	IDENTIFIER
Software and algorithms		
Origin	OriginLab Corporation	https://www.originlab.com
MATLAB	MATLAB Software Foundation	https://www.matlab.org
Photoshop	Adobe	https://www.adobe.com/products/photoshop

RESOURCE AVAILABILITY

Lead contact

Any additional information required to reanalyze the data reported in this work paper is available from the lead contact upon request, Hua-Jun Chen (chenphysics@126.com).

Materials availability

This work did not generate new unique reagents.

Data and code availability

All data reported in this paper will be shared by the lead contact upon request.

The code used in this study can be obtained in the supplemental information.

Any additional information required to reanalyze the data reported in this paper is available from the lead contact upon request.

METHOD DETAILS

Model and Hamiltonian

We designed a three-mode loop-coupled nanomechanical system that contains an NV center in diamond coupled to two nanomechanical modes via magnetomechanical interaction,[39] as shown in below figure.

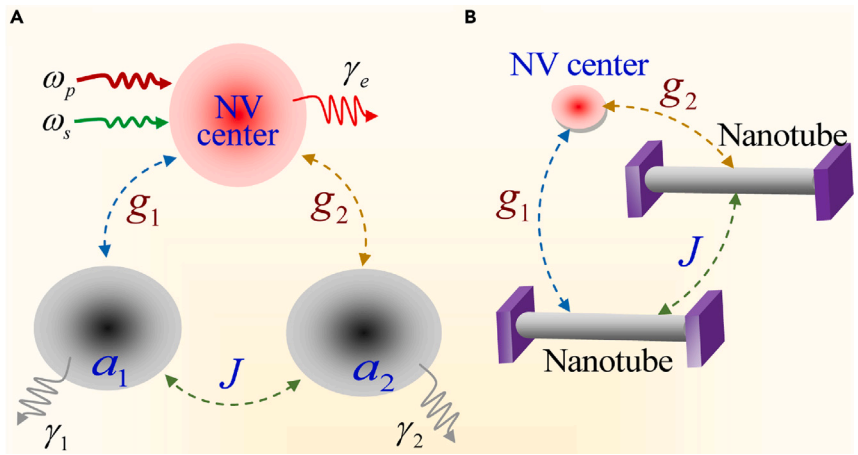

The model of the hybrid system

(A) Schematic diagram of the three-mode loop-coupled hybrid quantum system formed by an NV center in diamond (the NV spin is considered as a TLS with a decay rate γ_e) coupled to two mechanical modes a_1 and a_2 (with decay rates γ_1 and γ_2) with coupling strength g_1 and g_2.

(B) The two-mode coupled mechanical resonators can be realized by nanomechanical CNT resonators, which is coupled to a same NV center. The two CNT resonators are coupled to each other via a phase-dependent phonon-phonon interaction with the coupling strength J and the modulation phase θ, and the coupling of NV spin and two CNT resonators comes from the magnetomechanical interaction. The NV spin is driven by a strong pump field with frequency ω_p and a weak probe field with frequency ω_s.

The two nanomechanical modes are CNT resonators coupled to each other via phase-dependent phonon-exchange coupling[65] with coupling strength J and modulation phase θ.[88,89] For the two-mode coupling CNT resonators, we use creation (annihilation) operators $a_1^\dagger(a_1)$ and $a_2^\dagger(a_2)$ to describe them, the Hamiltonian of the two-mode coupling CNT resonators is $H_{CNT} = \sum_{k=1,2} \hbar\omega_k a_k^\dagger a_k$, where ω_1 and ω_2 are the frequencies of the CNT resonators with the decay rate γ_1 and γ_2. For the NV center in diamond, the NV spin can be considered as a TLS[14,18,33] with the ground state $|g\rangle$ and exciton state $|e\rangle$. We extract an NV spin couples to a CNT resonator of below figure,

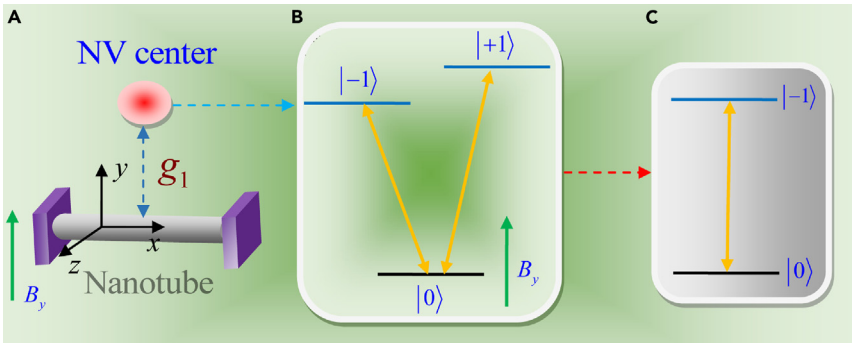

The two-level approximation of NV spin

(A) Schematic of a spin-mechanical system that contains an NV center in diamond coupled to a CNT resonator via magnetomechanical interaction.
(B) The energy level diagram of an NV center spin.
(C) The approximate two-level NV spin.

as shown in figure below, which is a typical spin-mechanical system. The NV center in diamond consists of a substitutional nitrogen atom and a vacancy, which own a spin $S = 1$ ground state with three substates $|m_s = 0\rangle$ and $|m_s = \pm 1\rangle$[39]. The three substates are separated by a zero-field splitting $D/2\pi = 2.87$ GHz between the states of $|m_s = 0\rangle$ and $|m_s = \pm 1\rangle$ as shown in Figure SB. When we apply a moderate static magnetic field $B = 300$ G[90] along the y direction, as shown in figure below, the degenerate spin states $|m_s = \pm 1\rangle$ can be removed, and the three-level NV spin is restricted to a two-level subspace covered by $|0\rangle$ and $|-1\rangle$[18], as shown in figure below. We use the Pauli operator $\sigma^z = |e\rangle\langle e| - |g\rangle\langle g|$ and the raising $\sigma^+ = |e\rangle\langle g|$ and lowering $\sigma^- = |g\rangle\langle e|$ operators to describe the TLS NV spin. Then the Hamiltonian of the spin is $H_{NV} = \frac{1}{2}\hbar\omega_e\sigma^z$ with the spin frequency ω_e of the NV center in the diamond.

The proposed hybrid quantum system can be carried out by photonic crystal cavity optomechanical systems,[65] electromechanical circuit systems,[60,91] waveguide-mediated distant mechanical coupling,[92] or the Coulomb interaction.[93–95] The phase-dependent phonon-phonon coupling, can be achieved by coupling to a charge qubit in electromechanical system[96] and has been demonstrated by two assistant cavity.[65] Furthermore, it was demonstrated that the phonon-phonon coupling between mechanical resonators can be controlled by gate voltage exerted on mechanical resonators in ion-nanomechanical systems,[50,97] where a gate voltage $V(t) = V_0\cos(\omega_{ac}t)$ with frequency ω_{ac} is exerted on NRs by Ohmic contacts. The charge on resonators vibrates with time and leads to oscillating forces on resonators.[97] We take the Coulomb interaction as an example to derive the interaction of two mechanical resonators.

We consider that the two CNT resonators with frequencies ω_1 and ω_2 take the charges C_1V_1 and $-C_2V_2$, where $C_1(C_2)$ and $V_1(-V_2)$ are the capacitance and the voltage of the bias gate, respectively. The Coulomb coupling of two CNT resonators is

$$H_{int} = \frac{-C_1V_1C_2V_2}{4\pi\varepsilon_0|y_0+y_1-y_2|}, \qquad \text{(Equation 1)}$$

where y_0 means the equilibrium distance of two resonators, y_1 and y_2 are the small displacements of two resonators from their equilibrium positions, respectively. Given $y_0 \gg y_1, y_2$, H_{int} can be rewritten as

$$H_{int} = \frac{-C_1V_1C_2V_2}{4\pi\varepsilon_0 y_0}\left[1 - \frac{y_1-y_2}{y_0} + \left(\frac{y_1-y_2}{y_0}\right)^2\right], \qquad \text{(Equation 2)}$$

with the second-order expansion, where the linear term is absorbed into the definition of the equilibrium positions, and the quadratic term includes a renormalization of the oscillation frequencies of CNT resonators. Then, we get a reduced form $H_{int} = \hbar J y_1 y_2$ with $J = \frac{C_1V_1C_2V_2}{2\pi\hbar\varepsilon_0 y_0^3}$. Considering $y_1 = a_1^\dagger + a_1$ and $y_2 = a_2^\dagger + a_2$ are the position operators of CNT resonators, then we get

$$H_{int} = \hbar J\left(a_1^\dagger + a_1\right)\left(a_2^\dagger + a_2\right). \qquad \text{(Equation 3)}$$

By ignoring the counter-rotating terms which do not conserve the number of excitations, the interaction Hamiltonian of CNT resonators is $H_{int} = \hbar J(a_1^\dagger a_2 + a_1 a_2^\dagger)$, and when a modulation phase θ is taken into consideration, then we obtain the Hamiltonian as

$$H_{int} = \hbar J\left(e^{i\theta} a_1^\dagger a_2 + e^{-i\theta} a_1 a_2^\dagger\right). \quad \text{(Equation 4)}$$

In the above rotating-wave approximation, the simplification is valid only in the regimes of the weak and strong coupling. If the mode coupling of two mechanical modes or a mechanical mode and a qubit reaches to the ultrastrong coupling regimes, the counter-rotating terms could not be ignored.[98] For spin-resonator interactions, under the rotating-wave approximation, the standard Jaynes-Cummings (J-C) Hamiltonian can be used to describe them[39] as

$$H_{S-R} = \sum_{k=1,2} \hbar g_k\left(a_k^\dagger \sigma^- + a_k \sigma^+\right), \quad \text{(Equation 5)}$$

Using the two-tone fields with frequencies of ω_p (pump field) and ω_s (probe field) to derive the TLS NV spin, the Hamiltonian[99] is

$$H_{dri} = -\sum_{j=s,p} \mu\varepsilon_j\left(\sigma^+ e^{-i\omega_j t} + \sigma^- e^{i\omega_j t}\right), \quad \text{(Equation 6)}$$

where ε_j is the slowly varying envelope, and we obtain the Hamiltonian of the entire system in a frame rotating pump field as

$$\begin{aligned} H &= H_{CNT} + H_{NV} + H_{S-R} + H_{int} + H_{dri} \\ &= \sum_{k=1,2} \hbar\omega_k a_k^\dagger a_k + \frac{1}{2}\hbar\Delta_p \sigma^z + \sum_{k=1,2} \hbar g_k\left(a_k^\dagger \sigma^- + a_k \sigma^+\right) + \hbar J\left(e^{i\theta} a_1^\dagger a_2 + e^{-i\theta} a_1 a_2^\dagger\right) - \hbar\Omega_p(\sigma^+ + \sigma^-) - \mu\varepsilon_s\left(\sigma^+ e^{-i\delta t} + \sigma^- e^{i\delta t}\right), \end{aligned} \quad \text{(Equation 7)}$$

with the spin-pump detuning $\Delta_p = \omega_e - \omega_p$, electric dipole moment μ, Rabi frequency $\Omega_p = \mu\varepsilon_p/\hbar$, and probe-pump detuning $\delta = \omega_s - \omega_p$.

Heisenberg-Langevin equations

According to the Heisenberg equation of motion, the Heisenberg-Langevin equations can be derived by adding the noise and damping terms as follows[100]:

$$\sum_{k=1,2} \dot{a}_k = -(i\omega_k + \gamma_k) a_k - i g_k \sigma^- - iJe^{i\theta} a_{3-k} + \hat{\xi}_k, \quad \text{(Equation 8)}$$

$$\begin{aligned} \dot{\sigma}^z = &-\gamma_e(\sigma^z + 1) - ig_1\left(a_1\sigma^+ - a_1^\dagger\sigma^-\right) - ig_2\left(a_2\sigma^+ - a_2^\dagger\sigma^-\right) \\ &+ i\Omega_p(\sigma^+ - \sigma^-) + \frac{i\mu\varepsilon_s}{\hbar}\left(\sigma^+ e^{-i\delta} - \sigma^- e^{i\delta}\right), \end{aligned} \quad \text{(Equation 9)}$$

$$\dot{\sigma}^- = -\left(i\Delta_p + \gamma_e/2\right)\sigma^- + 2ig_1\sigma^z a_1 + 2ig_2\sigma^z a_2 - 2i\Omega_p\sigma^z - \frac{2i\mu\varepsilon_s}{\hbar}\sigma^z e^{-i\delta} + \hat{f}, \quad \text{(Equation 10)}$$

where γ_1 and γ_2 are the decay rates of the two CNT resonators and γ_e is the decay rate of the NV spin.

$\hat{f}$ is the δ-correlated Langevin noise operator with zero mean $\langle\hat{f}\rangle = 0$ and obeys the correlation function $\langle\hat{f}(t)\hat{f}^\dagger(t')\rangle \sim \delta(t - t')$. The CNT resonators are affected by a Brownian stochastic force with the correlation function as

$$\langle\hat{\xi}^+(t)\hat{\xi}(t')\rangle = \frac{\gamma_k}{\omega_k}\int \frac{d\omega}{2\pi}\omega e^{-i\omega(t-t')}\left[1 + \coth\left(\frac{\hbar\omega}{2\kappa_B T}\right)\right], \quad \text{(Equation 11)}$$

with the Boltzmann constant k_B and the temperature T of the reservoir. In Equation 11, CNT resonators are affected by the thermal bath of Brownian and non-Markovian processes.[101] In low temperature, the quantum effects of phonon modes can be observed only in the case of resolved sideband regime, i.e., $\omega_1(\omega_2)/\gamma_1(\gamma_2) \gg 1$. In the weak coupling regime, the effect of Brownian noise is modeled as Markovian processes, additionally, the spin-resonator interactions are stronger than the coupling to the reservoir, considering the second order approximation,[101] the reservoir that affects phonon modes can be obtained as shown in Equation 11.

In order to solve Equation 8 to Equation 10, the perturbation theory $\rho = \rho_0 + \delta\rho$ (ρ_0 is the steady part and $\delta\rho$ is the fluctuation) was introduced and substituted into Equation 8 to Equation 10, a steady equation set can be obtained as follows:

$$\sum_{k=1,2} (i\omega_k + \gamma_k) a_{k0} + ig_k\sigma_0 + iJe^{i\theta} a_{3-k0} = 0, \quad \text{(Equation 12)}$$

$$i\Omega_p\left(\sigma_0^* - \sigma_0\right) - ig_1\left(a_{10}\sigma_0^* - a_{10}^*\sigma_0\right) - ig_2\left(a_{20}\sigma_0^* - a_{20}^*\sigma_0\right) = \gamma_e\left(\sigma_0^z + 1\right), \quad \text{(Equation 13)}$$

$$-\left(i\Delta_p + \gamma_e/2\right)\sigma_0 + 2ig_1\sigma_0^z a_{10} + 2ig_2\sigma_0^z a_{20} = 2i\Omega_p\sigma_0^z. \quad \text{(Equation 14)}$$

Solving Equation 12, the steady-state values of a_{10} and a_{20} can be obtained. Equations 13 and 14 together determine steady-state values of σ_0^z and σ_0. Especially, $\sigma_0^z \in (-1,0)$ and if $\sigma_0^z = -1$, the TLS NV spin is in its ground state.

Considering the pump field was sufficiently strong, using the mean-field approximation $\langle AB\rangle = \langle A\rangle\langle B\rangle$[81,102], the fluctuation operators will be identified with their expectation values. We obtain the Langevin equations of the expectation values by neglecting the nonlinear terms in the fluctuations as follows:

$$\sum_{k=1,2}\langle \delta\dot{a}_k\rangle = -(i\omega_k+\gamma_k)\langle\delta a_k\rangle - ig_k\langle\delta\sigma^-\rangle\langle -iJe^{i\theta}\rangle\langle\delta a_{3-k}\rangle, \tag{Equation 15}$$

$$\begin{aligned}\langle\delta\dot{\sigma}^z\rangle = &-\gamma_e\langle\delta\sigma^z\rangle - ig_1\left[\left(a_{10}\langle\delta\sigma^+\rangle+\sigma_0^*\langle\delta a_1\rangle\right)-\left(a_{10}^*\langle\delta\sigma^-\rangle+\sigma_0\langle\delta a_1^\dagger\rangle\right)\right]-ig_2\left[\left(a_{20}\langle\delta\sigma^+\rangle+\sigma_0^*\langle\delta a_2\rangle\right)-\left(a_{20}^*\langle\delta\sigma^-\rangle+\sigma_0\langle\delta a_2^\dagger\rangle\right)\right]\\&+i\Omega_p\left(\langle\delta\sigma^+\rangle-\langle\delta\sigma^-\rangle\right)+\frac{i\mu\varepsilon_s}{\hbar}\left(\sigma_0^*e^{-i\delta}-\sigma_0e^{i\delta}\right),\end{aligned} \tag{Equation 16}$$

$$\begin{aligned}\langle\delta\dot{\sigma}^-\rangle = &-\left(i\Delta_p+\gamma_e/2\right)\langle\delta\sigma^-\rangle+2ig_1\left(\sigma_0^z\langle\delta a_1\rangle+a_{10}\langle\delta\sigma^-\rangle\right)\\&+2ig_2\left(\sigma_0^z\langle\delta a_2\rangle+a_{20}\langle\delta\sigma^-\rangle\right)-2i\Omega_p\langle\delta\sigma^z\rangle-\frac{2i\mu\varepsilon_s}{\hbar}\sigma_0^ze^{-i\delta},\end{aligned} \tag{Equation 17}$$

Linear optical susceptibility

To solve the above equations, we consider the ansatz[99] as $\langle\delta\rho\rangle = \rho_+e^{-i\delta t}+\rho_-e^{i\delta t}$. Substituting these into Equation 15 to Equation 17, after ignoring the second-order terms and working in the lowest order in ε_s but for all orders in ε_p, the linear optical susceptibility can be obtained as $\chi_{eff}^{(1)}(\omega_s) = \mu\sigma_+(\omega_s)/\varepsilon_s = (\mu^2/\hbar\gamma_e)\chi^{(1)}(\omega_s)$. Here, $\chi^{(1)}(\omega_s)$ is

$$\chi^{(1)}(\omega_s) = \frac{\left[2\sigma_0^*\Omega_p-2i\sigma_0^z(\gamma_e-i\delta-\Pi_1\Pi_2)\right]\gamma_e}{\left[\Lambda_1-2i\sigma_0^z(g_1\beta_1+g_2\beta_2)\right](\gamma_e-i\delta-\Pi_1\Pi_2)-2i\Omega_p\Pi_3}, \tag{Equation 18}$$

with

$$\sum_{k=1,2}\beta_k = -\frac{ig_k(i\omega_{3-k}+\gamma_{3-k}-i\delta)+Jg_{3-k}e^{i\theta}}{(i\omega_k+\gamma_k-i\delta)(i\omega_{3-k}+\gamma_{3-k}-i\delta)+J^2}, \tag{Equation 19}$$

$$\sum_{k=1,2}\lambda_k = \frac{ig_k(-i\omega_{3-k}+\gamma_{3-k}-i\delta)+Jg_{3-k}e^{-i\theta}}{(-i\omega_k+\gamma_k-i\delta)(-i\omega_{3-k}+\gamma_{3-k}-i\delta)+J^2}, \tag{Equation 20}$$

$$\Lambda_1 = i\left(\Delta_p-\delta\right)+\gamma_e/2-2i(g_1a_{10}+g_2a_{20}), \tag{Equation 21}$$

$$\Lambda_2 = -i\left(\Delta_p+\delta\right)+\gamma_e/2+2i\left(g_1a_{10}^*+g_2a_{20}^*\right), \tag{Equation 22}$$

$$\Pi_1 = \frac{2i\Omega_p}{\Lambda_2+2i\sigma_0^z(g_1\lambda_1+g_2\lambda_2)}, \tag{Equation 23}$$

$$\Pi_2 = -i\left(g_1a_{10}+g_2a_{20}-\Omega_p\right)+i\sigma_0(g_1\lambda_1+g_2\lambda_2), \tag{Equation 24}$$

$$\Pi_3 = -i\left(g_1a_{10}^*+g_2a_{20}^*-\Omega_p\right)-i\sigma_0^*(g_1\beta_1+g_2\beta_2), \tag{Equation 25}$$

The imaginary and real parts of $\chi^{(1)}(\omega_s)$ manifest the absorption and dispersion, respectively.

Dark-mode effect

In the condition of the strong-driving regime, i.e., the pump field is more stronger than the probe field, according to the linearized Langevin equations of Equation 15 to Equation 17, the Hamiltonian in the rotating-wave approximation[85,88] is ($\hbar = 1$)

$$H_{RWA} = \frac{1}{2}\Delta_p\delta\sigma^z+\omega_1\delta a_1^\dagger\delta a_1+\omega_2\delta a_2^\dagger\delta a_2+g_1\left(\delta a_1^\dagger\delta\sigma^-+\delta a_1\delta\sigma^+\right)+g_2\left(\delta a_2^\dagger\delta\sigma^-+\delta a_2\delta\sigma^+\right)+J\left(e^{i\theta}\delta a_1^\dagger\delta a_2+e^{-i\theta}\delta a_1\delta a_2^\dagger\right). \tag{Equation 26}$$

In order to investigate the role of phonon-exchange interaction, two bosonic modes $\tilde{A}_+$ and $\tilde{A}_-$ are introduced as following

$$\tilde{A}_+ = f\delta a_1-e^{i\theta}h\delta a_2,\tilde{A}_- = e^{-i\theta}h\delta a_1+f\delta a_2, \tag{Equation 27}$$

then, the Hamiltonian of Equation 26 reduces to

$$H_{RWA} = \frac{1}{2}\Delta_p\delta\sigma^z + \tilde{\omega}_+\tilde{A}_+^\dagger\tilde{A}_+ + \tilde{\omega}_-\tilde{A}_-^\dagger\tilde{A}_- + \tilde{g}_+\left(\delta\sigma^-\tilde{A}_+^\dagger + \tilde{A}_+\delta\sigma^+\right) + \tilde{g}_-\left(\delta\sigma^-\tilde{A}_-^\dagger + \tilde{A}_-\delta\sigma^+\right), \quad \text{(Equation 28)}$$

where resonance frequencies and coupling strengths are as follows

$$\tilde{\omega}_\pm = \frac{1}{2}(\omega_1 + \omega_2) \pm \sqrt{(\omega_1 - \omega_2)^2 + 4J^2}, \quad \text{(Equation 29)}$$

$$\tilde{g}_+ = fg_1 - e^{i\theta}hg_2, \tilde{g}_- = e^{-i\theta}hg_1 + fg_2, \quad \text{(Equation 30)}$$

with the two parameters of

$$f = \frac{|\tilde{\omega}_- - \omega_1|}{\sqrt{(\tilde{\omega}_- - \omega_1)^2 + J^2}}, h = \frac{Jf}{\tilde{\omega}_- - \omega_1}. \quad \text{(Equation 31)}$$

When the two mechanical modes have the same frequencies, $\omega_1 = \omega_2$, and coupling strengths, $g_1 = g_1 = g$, the coupling strengths in Equation 30 can be simplified as

$$\tilde{g}_+ = \frac{\sqrt{2}g(1+e^{-i\theta})}{2}, \tilde{g}_- = \frac{\sqrt{2}g(1 - e^{-i\theta})}{2}. \quad \text{(Equation 32)}$$

In Equation 32, when $\theta = n\pi$ for an integer n, the spin mode is decoupled from one of the two hybridized mechanical modes $\tilde{A}_-$ (for an even number n) and $\tilde{A}_+$ (for an odd number n). These features mean that the dark-mode effect can be broken by tuning the modulation phase $\theta \neq n\pi$.

The light group velocity

The so-called slow and fast light conventionally indicate the group velocity of a light wave. The group velocity is closely related to the velocity at which a light pulse peak moves through an optical material, and is given by the standard result[79,80,103]

$$v_g = c/n_g, n_g = n + \omega\frac{dn}{d\omega}, \quad \text{(Equation 33)}$$

where n is the refractive index and ω is the angular frequency of the light field, and then $v_g \ll c$ means slow light, while $v_g > c$ indicates fast light. In our system, the group velocity changes to $v_g = c/[n + \omega_s(dn/d\omega_s)]$ with $n \approx 1 + 2\pi\chi_{eff}^{(1)}$, and we obtain

$$c/v_g = 1 + 2\pi Re\chi_{eff}^{(1)}(\omega_s)_{\omega_s=\omega_e} + 2\pi\omega_s Re\left[\frac{d\chi_{eff}^{(1)}(\omega_s)}{d\omega_s}\right]_{\omega_s=\omega_e}. \quad \text{(Equation 34)}$$

In the case of $Re\chi_{eff}^{(1)}(\omega_s)_{\omega_s=\omega_e} = 0$, the dispersion was steeply positive or negative, accompanied by significantly reduced or increased group velocities, respectively. To demonstrate the optical propagation property of the system, we introduce a group velocity index n_g as follows:

$$n_g = c/v_g - 1 = \frac{2\pi\omega_e\rho\mu^2}{\hbar\gamma_e}Re\left[\frac{d\chi^{(1)}(\omega_s)}{d\omega_s}\right] = \gamma_e\Phi Re\left[\frac{d\chi^{(1)}(\omega_s)}{d\omega_s}\right], \quad \text{(Equation 35)}$$

with $\Phi = 2\pi\omega_e\rho\mu^2/\hbar\gamma_e^2$, where ρ is the density of spin-CNT resonators. Thus, we refer to slow light as $n_g > 0$, fast light as $n_g < 0$[79,80].

QUANTIFICATION AND STATISTICAL ANALYSIS

Our study does not include statistical analysis or quantification. In this work, through rigorous theoretical derivation, we obtain the Equations 18 and 35 in the section of method details. Based on Equations 18 and 35, and according to the system parameters, we make numerical simulation by MATLAB software. Although the simulation data is produced by MATLAB software from Figures 1, 2, 3, 4, 5, 6, 7, 8, and 9 (for the codes, see the supplemental information), figures shown in the main text were produced by ORIGIN from the raw data. In addition, in the simulation, the system parameters are as following: the frequencies of CNT resonators $\omega_1 = \omega_2 = 65$ MHz (or $\omega_1 \neq \omega_2$), the spin-resonator coupling strength $g_1 = g_2 = 4.5$ MHz, the decay rates of the CNT resonators $\gamma_1 = \gamma_2 = 15$ kHz, the Rabi frequency $\Omega_p = 10$ (MHz)^2, the decay rate of the NV spin $\gamma_e = 60$ MHz, the range of the phonon-phonon coupling strength belongs to $J \sim [10, 100]$ MHz with the modulation phase $\theta \in [0, 2\pi]$. By the way, nanomechanical resonators with high frequencies ranging from 100 MHz to a few GHz have been realized in the mechanical devices with smaller sizes or greater stiffness at present, which indicates potential applications in nanoscale. Moreover, the diagrammatic figures of Model and Hamiltonian section are drawn by Photoshop software.